Continental Shelf Research
March 2001, Volume 21, Issue 4, Pages 423-454
http://dx.doi.org/10.1016/S0278-4343(00)00090-X

Simulating vertical mixing in a shelf-break region: addition of a shear instability model, accounting for the overall effect of internal tides, on top of a one-dimensional turbulence closure mixed layer model

J. N. Druon [a, 1, *], G. Langlois[b] and J. Le Fèvre[a]

[a] Laboratoire Flux de Matière et Réponses du Vivant, UMR 6539, Université de Bretagne Occidentale, Institut Universitaire Européen de la Mer, Technopôle Brest-Iroise, Place Nicolas Copernic, 29280 Plouzané, France
[b] ADHOC (Agence pour le Développement en Hydrodynamique et Océanographie Côtière) 20 Quai Malbert, 29200 Brest, France
[1] Present address: IFREMER, Centre de Brest, Département d'Ecologie Côtière, Eutrophisation et Bioaccumulation, BP 70, 29280 Plouzané, France

*: Corresponding author: Tel.: +33-2-98-22-44-75; fax: +33-2-98-22-45-48; email: jean.noel.druon@ifremer.fr

Abstract:

A simple parameterization of eddy diffusivity is used to simulate the shear mixing from tidally induced internal waves generated in the continental slope region southwest of Brittany. Near the edge of the shelf, the seasonal thermocline oscillates under the forcing of the barotropic tide which propagates over the shelf break. A composite model is constructed to simulate the mixing of the upper ocean from both external (wind stress) and internal (internal waves) sources. A simple one-dimensional eddy kinetic energy model, which predicts the temperature profile from heat flux and wind stress inputs, is validated with respect to regional hydroelimatic conditions, then coupled with a two-layer model of non-linear internal waves, to simulate the mixing encountered in shelf break fronts submitted to tidal forcing. Numerical runs on a transect perpendicular to the shelf break show the formation of a spot of cool water over the edge of the continental margin. The one-dimensional eddy kinetic energy model has been validated over a decade with temperature profiles over the abyssal plain adjacent to the continental slope. An annual validation experiment has also been conducted for the combined models, beginning on 1st January 1985, as well as a short-term validation experiment, using a set of high-frequency temperature measurements at two stations near the shelf edge in September and early October 1985. The simulation has also been spatially validated against three sets of infrared satellite images. The one-dimensional model is calibrated for the minimum turbulent kinetic energy, whereas the best fit to the high-frequency measurements in autumn 1985 above the slope provides the optimum values for the initial thermal content and for the parameterization constant of internal wave diffusivity. The combined model reproduces successfully the seasonal and the high-frequency (neap-spring tidal cycle) variation of the temperature field in the upper ocean along a transect perpendicular to the shelf break. Horizontal advection and mesoscale turbulence somewhat limit the performance of the model at low-amplitude tides and over the shallower part of the shelf, but the satisfactory overall agreement between the results and the measurements is consistent with the formation of a shelf break front in the northern Bay of Biscay and southern Celtic Sea, mainly as a result of mixing enhanced by tidally induced internal waves.

Keywords: Vertical mixing; Shelf-break; Wind stress; Internal waves; ECWMF fluxes; Bay of Biscay (47°N; 6°W)

Introduction

At the time of the year when the seasonal thermocline is established, the surface waters are consistently cooler, by about 2°C, over the northern continental slope of the Bay of Biscay than over both the shelf and the abyssal plain. This feature has been attributed by a number of authors (Pingree, 1978; Dickson et al., 1980; Heaps, 1980, Johnson and Nurser, 1983, 1984) to some kind of Ekman upwelling. The phenomenon, however, is now known to be associated with the generation of internal waves, which have even been directly observed on one exceptional scene from satellite-borne radar imagery (Pingree and Mardell, 1981). It was first proposed by Mazé (1980) that the interaction between bottom topography and the propagation of the barotropic tidal wave would generate an internal (baroclinic) tide, i.e. internal waves with a tidal periodicity, over the shelf break. Further studies (Pingree et al., 1984; Mazé et al., 1986; Mazé, 1987; New and Pingree, 1990) have confirmed the hypothesis and shown the internal tide to be strongly non-linear, especially in the region of its generation, over the shallower part of the slope. These waves were suggested to be an important source of vertical mixing. Recently again, Gekerma and Zimmermann (1995) have shown that a two layer model is sufficient to reproduce the non-linear characteristics of such internal motions. At the phase of the oscillation when the thermocline is nearer the surface, the interaction with wind stress results in enhanced vertical mixing. Internal tides are generated in various slope areas throughout the world ocean (Baines, 1982), as in the Australian north west shelf (Holloway, 1994 and 1996), and in the Malin-Hebrides shelf (Xing and Davies, 1996 and 1998a). The regions of intense surface and bottom turbulence associated with internal tides are found in the shelf break area. The recent work of Xing and Davies (1996) has shown that internal tidal mixing can reach the sea surface at the shelf edge even without wind mixing. The influence of the eddy diffusivity parameterization in mixing processes associated with internal waves is thus a prerequisite to the construction of a realistic model of the phenomenon as observed in situ. The comparison of simulated internal tides in which the eddy viscosity and diffusivity were determined using an algebraic formulation depending upon a Richardson number with those computed using a two equation ($q^2 - q^2 l$) turbulent energy model did not reveal any significant differences (Xing and Davies, 1997 and 1998b). Biological consequences of the internal tide regime may range from increased biological production (due to the upward

flux of nutrients from below the euphotic zone associated with the local mixing, and the increased amount of available light in relation with the internal wave oscillation) in some major fisheries region (the northern Bay of Biscay itself: Holligan et al., 1985, Le Fèvre and Frontier, 1988; the Atlantic approaches of Canada: Sandström and Elliott, 1984; the shelf break off Argentina: Podestá and Esaias, 1988; California: Shea and Broenkow, 1982) to the transport of invertebrate larvae to their settling grounds through special circulation features associated with internal tides (Pineda, 1991).

The present work was part of an attempt to study, and quantify, the influence of mixing enhanced by internal waves on pelagic ecosystems at the seasonal scale (Druon, 1998; Druon and Le Fèvre, 1999). This requires a relatively robust, low-cost simulation of the physical forcing, exhibiting sufficient stability at the annual or interannual scale. In this context, the vertical mixing regime in the region is simulated by combining two different models. The 1-D model of eddy kinetic energy of Gaspar et al. (1990) is used to account for the overall effect of physical forcing (wind stress and heat fluxes) along the vertical. This model is first validated for the hydroclimatic conditions over the abyssal plain adjacent to the continental slope. It is then coupled with a two-layer model of internal waves, using the 2-D numerical results of Mazé (1987), to account for the specific, additional effect of internal waves on the vertical heat and nutrient fluxes. The eddy kinetic energy (TKE) model for simulations of the oceanic vertical mixing described in Gaspar et al. (1990), hereafter referred to as GGL, is rather simple and efficient under wind stress and heat flux forcing. This model was first validated by the authors at Station Papa in the Gulf of Alaska and in the Sargasso Sea, using moorings of the Long-Term Open Ocean Study (LOTUS). It was also validated in the Southern Ocean by Pondaven et al. (in press), and coupled to ecosystem models in different regions of the world ocean (Southern Ocean: Pondaven et al. (1999), Sargasso Sea: Marchal et al. (1996)). The GGL model uses a single prognostic equation for the turbulent kinetic energy (TKE). The model of Mazé allows for the simulation of the generation and propagation of non-linear internal waves being induced over a shelf break as a result of the propagation of the barotropic tidal wave in a two-layer ocean. The cornerstone of the coupling between the two models is the parameterization, in the form of a specific eddy diffusion coefficient, of the effect of internal waves on vertical mixing along a vertical transect normal to the slope. In this frontal area, many authors have shown qualitatively that the vertical physical and biogeochemical

structures are deeply modified by internal waves. This work tends to complement these previous studies by giving a quantitative approach.

1 Regional validation of the eddy kinetic energy model

1.1 Validation data sets

To improve the parameterization of the turbulent diffusion and to set the proper values for the parameter calibration, a set of ten years of data has been choosen rather than a climatological data set.

The solar flux, non-solar fluxes (the sum of the sensible, latent and net infrared heat fluxes) and wind at 10 m have been provided by Météo-France and have been extracted from the European Center for Weather and Meteorological Forecast (ECWMF) model. The 6-hourly data cover the period 1985-1994, and correspond, in the 1^o by 1^o grid, to the point of coordinates 47^oN, 6^oW.

The annual heat budgets are balanced with an additional mean term to the non-solar flux, in order to prevent a divergence of the heat content when repeating the same year of simulation (spin-up), and to obtain a realistic initial condition. The heat budget over ten years is almost closed (Fig. 1), and the net annual imbalance does not exceed 11 W m^{-2} in 1992, which corresponds to 8% of the mean solar flux. As mentioned by Archer (1995), the oceans transport heat from low latitudes to high latitudes, so that only in mid-latitudes can the heat fluxes be expected to balance locally (Peixoto and Oort, 1992). A major uncertainty in the heat balance of the surface ocean is represented by the effect of clouds (Seager et al., 1998; Wigley, 1989; Mitchell et al., 1989). The interannual standard deviation of the total heat flux has been estimated to be on the order of 25 W m^{-2} (Weare et al., 1981; Davis et al., 1981; Seager et al., 1988). This further justifies, in the north of the Bay of Biscay, the balancing of annual heat budgets and the use of a one dimensional model for a multi-annual simulation (low long-term oceanic heat transport towards the north). The solar flux is first dayly integrated, and then distributed with a time step of 600 s, taking into account the total energy and the duration of day-time along the year. Solar and non-solar fluxes are spline-cubic interpolated with the same time step.

Wind direction and velocity are interpolated independently. It must be underlined that the

type of wind measurements from weathership station Papa used by Gaspar et al. (1990) for their model validation is rather different from the outputs of the ECWMF model. The 3-hourly wind speed given at Station P in the subarctic Pacific or at Station K in the North Atlantic results from the integration of measurements over 2 or 3 minutes, while the wind speed given by the ECWMF model is representative of the mean stress over the entire 6-hour period. The comparison of the mean wind speed given at Station K (45°N, 18°W) in 1975 (9.25 m s^{-1}) with the decadal mean wind speed at the same point given by the ECWMF model from 1985 to 1994 (8.22 m s^{-1} with a standard deviation of 0.23 m s^{-1}) leads to a mean wind speed decrease of 12.5%. This difference (in absolute terms) is increased by a square power when calculating the wind stress (26.5%).

The temperature measurements have been collected through the SHOM (Service Hydrographique et Océanographique de la Marine) data base in the area 46 - 48 °N, 5 - 8°W between 1985 and 1994 (hatched zone in Fig. 2). Each temperature profile has been linearly interpolated between the surface and 125 m with a vertical step of 5 m. At this stage, any effect from internal waves would introduce a bias in the validation of the GGL model. The stations retained here for the validation are accordingly located 50 km off the generation zone, centered on the top of the shelf break, of the internal waves to minimize their effect as much as possible.

1.2 Initialization and numerical implementation

The initial condition on January 1^{st} 1985 is set by doubling the first year of simulation. The absorption law for the solar irradiance is parameterized according to Paulson and Simpson (1977) for a water optically intermediate between Jerlov's (1968) type I and type II. The values of R and ζ_1 are the same as for water type I, with the adjustment of $\zeta_2 = 12$ m instead of 23 m to fit the measurements of Le Cann and Cabillic (1979) carried out on the shelf south of Brittany in November 1978, with a non-zero chlorophyll content in the sea water. This law is similar to water type I in the top 5 m, but the influence on the temperature profile is not important because of the high wind mixing, and similar to water type II below 30 m. A test simulation was performed with a biogeochemical model to evaluate the impact of chlorophyll concentration on surface temperature, using the formulation of the light extinction coefficient given by Parsons et al. (1984). The results showed a maximum increase of surface temperature on the order of 0.1°C during the warmer month of the year (September). This slight biological

feedback on the physics was not retained in the final simulation.

The salinity is considered constant in the simulations. The usual salinity gradient observed in the study area is smaller than 0.1 psu in the top 200 m, with a surface value of 36.65 psu. The higher salinity at the surface results from the evaporation-precipitation budget.

The model's equations are finite differenced on a staggered grid, i.e., temperature and the horizontal components (T, u and v) of the velocity are computed at the center of each grid cell while the turbulent fluxes and TKE are determined at the cell boundary. This 1D-vertical model has a time step of 600 s, a spatial resolution of 2.5 m, and describes the upper 250 m of the water column.

1.3 Calibration

The purpose here is to minimize the mean distance between the measured and simulated temperature in the first 120 m of the water column on a decadal simulation. The root mean square (RMS) of the temperature difference between the model and the measurements has been calculated from the surface to 120 m with a vertical resolution of 5 m. Two parameters need to be calibrated to fit the model to the measurements: the initial condition and the minimum of turbulent kinetic energy (TKEm). The initial condition Θ_i is the temperature of the homogeneous profile used at the beginnig of the spin-up, and, because of the closed heat budget, it represents the initial thermal contents in the domain of calculation at the end of the spin-up. The minimum of the root mean square (RMS) of the temperature difference between the model and the measurements yields the optimum values of $\Theta_i = 12.30\ ^{o}$C and TKEm $= 10^{-5}$ m^2 s^{-2}.

1.4 Results

Figures 3, 4 and 5 represent, for the period 1985-1994, the comparison of the in situ and model temperature at 5, 50 and 120 m, respectively, using balanced annual heat budgets (a), and the original ECWMF heat fluxes (b). The temperature difference at 5 m between the simulation and the measurements, hereafter called ΔSSTs, is presented in Fig. 6 both for a balanced and non-balanced annual heat budget. The simulation which uses the non-balanced ECWMF fluxes shows an interannual temperature variation which is less correlated with the

measurements at the surface and at 120 m (Figs. 3 and 5) than in the balanced budget case, with a very clear positive anomaly (simulation higher than the measurements) at the surface since 1991 (Fig. 6). Part of this divergence might come from slight errors in the estimation of the cloud cover, and its influence on heat fluxes. The high ΔSSTs encountered in 1991 and 1992 could be related to the information contained in the atmospheric fluxes concerning the influence of El Niño Southern Oscillation (ENSO). Other sources of short-term (< a few months) discrepancy between the 1D model results and the measurements are the horizontal advection from the tidal current, and the macro-turbulent advection of large gyres which occur frequently along the slope of the Bay of Biscay, exporting cooler water from the top of the shelf break towards the west (Deschamps et al., 1984; Pingree and Le Cann, 1992 (a); Pingree and Le Cann, 1992 (b); Druon, 1995).

The quantitative results are synthesized in the Fig. 7. The RMS comparison over the decade between the balanced and non-balanced heat budgets reveals a difference of standard deviation of 0.2 ^{o}C near the surface and at 120 m. Even if the annual heat imbalance is small in the study area, a better simulation of the temperature in the upper ocean is achieved with balanced annual heat budgets. The high values of RMS observed in the vicinity of 50 m result from the residual effect of the internal waves. This oscillation of the thermocline shows up through the large temperature variability observed at the same time at 50 m during the warm season (Fig. 4). As shown below, internal waves are generated near the top of the shelf break, and, considering their large wavelength (30 km), they partially propagate beyond 50 km off the generation zone. In order to remove as much as possible the influence of the internal waves from the validation of the model, the parameters Θ_i and TKEm were calibrated in such a way that the simulated surface temperatures were adjusted to the warmer measurements in the area (hatched part in Fig. 2). In addition, the minimum profile of RMS of the temperature difference between the measurements and the model has been calculated to choose the values for TKEm and Θ_i using the values obtained from the surface to 30 m, and from 60 to 120 m. Thus, the large temperature range observed in the measurements near 50 m (Fig. 4), which results from the propagation of internal waves across the area selected in the hatched area of figure 2, were not used to calibrate the TKE one-dimensional model which is not simulating tidal processes. This leads to a degradation of the RMS profiles and the ΔSSTs. Excluding the interannual variability, an annual positive anomaly of ΔSST is detected from May to

September (Fig. 6). In the same context, the annual RMS show a slight increase at the surface. A large interannual variation of the difference between the model and the measurements is found in the RMS profiles (Fig. 7). A much better fit, for instance, is obtained in 1988 than in 1994 (Figs. 8 - 9). The comparison between the two figures (middle and bottom graphs) shows that part of the difference is probably due to the much more uneven spatio-temporal distribution of the measurements in 1994 compared to 1988.

As shown in Fig. 10, the eddy diffusivity coefficient in 1985 shows a large seasonal variability, with strong winter and low summer wind mixing. These seasonal values of the eddy diffusivity K_h are similar those obtained by Gaspar et al. (1990) (their Fig. 3, Station Papa, 1969), except towards the low values ($K_h = 10^{-5}$ m^2 s^{-1}) at the thermocline level, because of the higher TKEm used in the present study (TKEm = 10^{-5} m^2 s^{-2} instead of 10^{-6} m^2 s^{-2} in Gaspar). This difference in values of TKEm has several reasons. The negative downward gradient of salinity induces in the real world a higher vertical gradient of density and thus higher mixing. This effect was not taken into account in the present study, and has to be compensated for in the value of TKEm. In addition, the difference in the types of wind measurements, as discussed above, leads to wind speeds stronger by 12.5% on the average in the weathership data base used by Gaspar than in the data set used in the present model. This large overestimation of the weathership wind speeds leads Gaspar et al. (1990) to lower their TKEm value to fit the temperature measurements at Station Papa. Finally, a bias is introduced here by the spatio-temporal distribution of the stations (hatched part in Fig. 2, Figs. 8 and 9). The climatological atlas of the Bay of Biscay (SHOM) indicates a mean horizontal gradient of surface temperature of 0.5 °C in the hatched part of Fig. 2, which explains a significant part of the errors.

In their sensitivity analysis, Gaspar et al. (1990) ran their model with the same TKEm value as used here (10^{-5} m^2 s^{-2}), and this led to an overestimation of the vertical heat diffusivity at Station Papa. But these authors also suggested that large mixing rates detected just below the mixed layer after strong wind events, as observed by D'Asaro (1985) and Large et al. (1986), should require a parametrization of TKEm at these depths as a function of the wind forcing. This locally enhanced mixing is needed to reduce the stratification in the upper thermocline produced during summer and early fall by the model of Gaspar et al. (1990). In the present work, the high TKEm value induces this autumnal mixing and, during the stratification

period, provides an adjustment to the mixing due to the salinity gradient. A best simulation was fitted to a situation including a mean salinity gradient of -0.1 psu at the top 200 m (results not shown). This allowed a decrease of the TKEm value to 4.10 $^{-6}$ m^2 s^{-2}, but the RMS profile for the decade was still at least twice higher than in the reference simulation (constant salinity and TKEm = 10 $^{-5}$ m^2 s^{-2}). This divergence with the measurements is due to a temporal variability of the salinity profile. In view of the available measurements, the latter seems to show a persistent relative vertical gradient, but the absolute values oscillate with an amplitude of $\pm$ 0.05 psu.

2 Mecanisms of the coupled models - Vertical mixing parameterizations

The shelf break area off Brittany is characterized by a low residual tidal current and by strong wind mixing. A 1-D vertical model is thus an acceptable approximation to describe the upper ocean physics. Salinity has a low vertical gradient in the top 250 m, and is considered constant (the budget Evaporation - Precipitation = 0). The TKE equation and the conservation of momentum are detailed in Appendix A. The background concerning the TKE closure and the turbulent length scales is described by Gaspar et al. (1990).

2.1 The equation of heat

In the one-dimensional case the conservation of heat yields

$$\frac{\partial T}{\partial t} - \underbrace{\Phi(z)}_{1} - \underbrace{\frac{\partial}{\partial z}\left(K_h \frac{\partial T}{\partial z}\right)}_{2} = 0 \qquad (1)$$

where T is the temperature, K_h is the eddy diffusivity coefficient for heat under the effect of the surface wind, and the underlined terms in Eq. (1) are respectively:
1- the solar irradiance absorbed at the depth z,

$$\Phi(z) = \frac{F_{sol}}{\rho_0 c_p} \frac{\partial I}{\partial z}$$

where F_{sol} is the solar irradiance absorbed at the surface, ρ_0 and c_p are the reference density and specific heat of seawater respectively, and $I(z)$ is the fraction of F_{sol} that penetrates to depth z;

2- the gradient of the turbulent heat flux (diffusion). The boundary conditions associated to this differential form are:

$$K_h \frac{\partial T}{\partial z}\bigg|_0 = F_{nsol} \quad ; \quad K_h \frac{\partial T}{\partial z}\bigg|_{-H} = 0 \tag{2}$$

where H is the maximal depth of calculation, and F_{nsol} is the "nonsolar" heat fluxes, i.e., the sum of the sensible, latent and net infrared heat fluxes.

2.2 Modelling the internal waves

2.2.1 The tidal wave model and the two-layer scheme

At the level of the thermocline, the effect of internal waves is represented by the oscillation of a virtual interface (a schematic discontinuity of the density profile) separating two homogeneous layers. The current shear from the interface oscillation is the main source of internal turbulence in the water column. The characteristics of the interface is estimated with a two-layer scheme of the discrete density profile using, as a stationary state, the conservation of internal and potential energy. The numerical model of internal waves of Mazé (1987) is used to describe the evolution of the two-layer interface and the associated shear currents on a vertical transect across the shelf break. The tidal solution used to force the two-layer model is described in Le Tareau and Mazé (1996).

2.2.2 The numerical model, parameterization

The effect of internal waves is introduced by the following equation for the conservation of heat:

$$\frac{\partial T}{\partial t} - \underbrace{\Phi(z)}_{1} - \underbrace{\frac{\partial}{\partial z}\left[(K_h + K'_h)\frac{\partial T}{\partial z}\right]}_{2} = 0 \tag{3}$$

The term underlined 1 is the same as explained above. A second complementary term to the classical concept of eddy diffusivity, which cannot be introduced on a more precisely deterministic way, reflects the turbulent mixing caused by internal waves (expression 2). In the classification of mixing models of Archer (1995), the model of GGL is a "turbulence closure model", and the internal mixing model presented here is a "shear instability model". The latter, which provides a parameterization of K'_h, uses the generation of turbulence by current shear as a source of TKE. The parameterization of the diffusivity coefficient K_h is described by

Gaspar et al. (1990). The eddy diffusivity coefficient associated to internal waves K'_h, is expressed by a hybrid form (see below). The unstability effect results from the current shear of a two-layer dynamical solution of tidally generated, propagating internal waves. The boundary conditions associated to this parameter are:

$$K'_h \frac{\partial T}{\partial z}\bigg|_0 = 0 \quad ; \quad K'_h \frac{\partial T}{\partial z}\bigg|_{-H} = 0 \tag{4}$$

Turner (1981) has shown that, in the water column, mixing mecanisms depending of turbulence from an internal or an external source are different. Although, in the present work, the eddy diffusivity caused by internal waves and the eddy diffusivity due to surface wind stress are treated as homogeneous quantities, the expression of K'_h is different from GGL's expression for K_h. As indicated in Gargett (1984), and Gargett and Holloway (1984), the turbulent diffusivity reflecting the vertical mass transport caused by internal oscillations is proportional to N^{-q} with $q \sim 1$, assuming a steady-state wave kinetic energy. Under this condition, these authors define a Richardson number associated to internal wave motions $Ri_w \sim 0(1)$ with:

$$Ri_w \equiv \frac{N^2}{(\frac{\partial u_i}{\partial z})^2}, \tag{5}$$

where $u_{i=1,2}$ is the horizontal current induced by internal waves, and $N \equiv ((-g/\rho_0)\frac{\partial \rho}{\partial z})^{\frac{1}{2}}$ is the Brunt - Väisälä frequency. When the Richardson number reaches a value lower than the critical value R_{ic}, the current shear generates Kelvin-Helmotz instabilities which increase mixing at the level of the thermocline. Commonly, R_{ic} is set to 1/4.

An instantaneous interfacial Richardson number is introduced here to describe the internal wave mixing of the two-layer dynamical system:

$$Ri_b = \frac{g' h_1}{(\Delta u)^2} \tag{6}$$

where h_1 is the thickness of the mixed layer, $(\Delta u)^2 = (u_2 - u_1)^2$, with u_1 and u_2 the upper and lower current velocity respectively, and g' the reduced gravity associated with buoyancy, i.e. $g' = g\alpha_T(T_1 - T_2)$, where g is the force of gravity, α_T the heat expansion coefficient, and T_1 and T_2 the upper and lower layer temperature respectively.

The two-layer Richardson number is not constant with respect to the instantaneous state of wave kinetic energy, and numerical simulations even show situations where $R_{ib} > 1$. In the case of the two-layer dynamical system, the "internal Richardson number", or "bulk Richardson

number" (Pollard et al., 1973; Price et al., 1986) does not reach the critical value because the two-layer approximation is no longer valid when the thermocline vanishes.
The eddy diffusivity K'_h is formulated as:

$$K'_h = \kappa_h (1 + aRi_b)^b \tag{7}$$

The validation of this expression is reviewed by Rodi (1993), who also gives the mean values for a (= 10/3) and b (= -3/2). The parameter κ_h is a function of z, and reflects the effect of internal oscillations on the vertical density structure. On a first approximation, the internal eddy diffusivity coefficient is expressed, in the two-layer scheme, as $K'_h \equiv \kappa_h (aRi_b)^b$. Using the general form of the Richardson number (Ri_w), this coefficient can be written as a function of the buoyancy frequency: $K'_h \equiv \kappa_h (aRi_w)^b \equiv \kappa_h (\frac{N^2}{(\frac{\partial u_i}{\partial z})^2})^{-\frac{3}{2}} \equiv \kappa_h \frac{N^{-3}}{(\frac{\partial u_i}{\partial z})^{-3}}$. To take into account the dependency of K'_h on N^{-1} (Gargett, 1984), the following expression has been adopted:

$$\kappa_h = C_\sigma N^2 \tag{8}$$

where C_σ is the calibration constant of this parameterization. The stability due to stratification ($N^2(z,t)$) is evaluated with the temperature profile obtained with Eq. (1). The unstability effect is estimated through the shear velocity $(\Delta u(x,t))^2$.
The characteristics of the two-layer profile (g' and h_1) are deduced from the discrete vertical profile using the conservation of potential energy and internal energy (see Appendix B). The relations between the two models are illustrated by Fig. 11. The coupling is performed through the calculation of g' and h_1 every 24 h, and through the calculation of $K'_H(x,z)$ which includes the two-layer Richardson number at point x and the buoyancy frequency at depth z.

3 Configuration of the coupling

The schematic configuration selected for the analytical and numerical study of the coupled model is presented in Fig. 12. The continental shelf break has a length of $\mathcal{L}$ = 38 km, and a slope $\alpha = 0.1$. The linear barotropic tide is represented by two monochromatic waves of period T_1 = 12.00 h (S_2) and T_2 = 12.42 h (M_2), and is established according to the method of Le Tareau and Mazé (1996). This method, elaborated to prevent difficulties due to bathymetric discontinuities, allows the coupling to escape analytical problems near the edge of the shelf. A

continuous solution for the tide can be calculated at the upper limit of the shelf break using a continuous topography. The form of the topography used in the calculations is $[(\sin x)/x]^2$, with x the axis coordinate perpendicular to the shelf break. The maximum amplitude of the tidal current is located near the top of the shelf break and reaches 0.5 m s^{-1} (Fig. 13). The maximum of barotropic forcing is located approximately 3 km off of the top of the shelf edge (Fig. 14), and tidal propagation at this point induces a vertical current of 0.2 cm s^{-1} at the depth of 30 m.

4 Simulations at the shelf break off-shore of Brittany

4.1 Choice of the data set

Two different sets of data are needed to calibrate and validate the model. The validation and calibration of the GGL model have been discussed above. The measurements needed to calibrate a model reflecting the mixing by turbulent diffusion of internal waves require a high frequency (15 to 30 min.). Autumn is the period when internal waves influence most the physics of the water column, and the time span of the measurements must be long enough to cover 1 or 2 spring-neap cycles. Moreover, measurement stations must be located on a transect normal to the shelf break, and on several tens of kilometres on each side of it. Data from thermistor-chains collected during the oceanographic cruise ONDINE 85 of the SHOM almost meet such requirements. The temperature from 0 to 105 m was measured with a frequency from 5 to 20 minutes during 40 days, beginning 6^{th} September 1985. Only 2 stations, however, have been sampled on the same transect at less than 20 km from the top of the shelf break. Station P1 is located at 1 km in shore of the top of the shelf break (47^o36.2'N, 7^o14.1'W) and Station P2 is at 2 km in shore from P1 (47^o36.15'N, 7^o12.35'W) (Fig. 2). A set of AVHRR SST (Advanced Very High Resolution Radiometer Sea Surface Temperature), integrated on the transect (Mazé and Langlois, 1992), were used to spatially complement the validation. The 6-hourly values of the surface wind stress τ (shown partially in Fig. 15) and heat fluxes (F_{sol}, F_{nsol}) from the ECWMF model at the point 47^oN, 6^oW. The annual heat budget of -5.7 W m^{-2} in 1985 has been balanced with an additional constant term to the "nonsolar" fluxes. All the background concerning the heat fluxes and the wind stress is discussed above.

4.2 Initialization and numerical implementation

The simulations include the two semi-diurnal waves M2 and S2 during the year 1985, which is simulated twice to start the calculation on 1^{st} January with realistic profiles of temperature and TKE. The two-layer dynamical model is activated on 15^{th} May when a significant thermocline (density gradient) appears, and runs as long as the latter is found (31^{st} December). The characteristics of the two-layer profile g' and h_1 are recalculated every 24 h. The diffusive effect of internal waves is estimated without directly taking into account the vertical alternative advection. The instantaneous model outputs of temperature, driven by the parameterization of K'_h, do not lead to the oscillation of the thermocline forced by tidal currents, but is representative of a mean situation of the temperature distribution under the forcing of the additional internal diffusion. In order to obtain comparable measured and calculated temperatures, measurements and outputs of the model are integrated over two M2 periods (24.84 h). Thus, this process eliminates the main tidal oscillation, despite phase differences of other waves which are not included in the model. Temperature results are compared at two points of the transect (see Fig. 2: P1 and P2).
The simulation is performed using a uniform vertical resolution of 2.5 m from the surface down to 200 m above the shelf, and 250 m in deeper waters. The time step is 600 s.

4.3 Calibration

The calibration of the minimum of turbulent kinetic energy (TKEm) was realized over a decade and has for optimal value 1. 10^{-5} m^2 s^{-2}. Two parameters need to be calibrated to fit the results of the coupled model to the measurements: the initial condition and the specific parameterization coefficient of the internal diffusion (C_σ). Few measurements are available near 1^{st} January 1985, but the climatological atlas of SHOM shows, in January, a temperature gradient of 0.5^{o}C between the shelf break area (cooler) and above the abyssal plain (warmer) in the top 50 m. The optimal value for Θ_i in the abyssal plain area was found above to be 12.30 ^{o}C. The minimum of the root mean square (RMS) of the daily integrated temperature difference between the model and the measurements at P1 and P2 yields the optimum values $\Theta_i = 11.85$ ^{o}C and $C_\sigma = 200$ m^2 s.

4.4 Results and discussion

Figure 16 shows the temporal variations of temperature calculated at three depths over the top of the shelf, with the validation data superimposed. The latter are extracted from the SHOM data set in a 50 km belt extending offshore from the 200 m isobath (non-hatched area in the reference square on Fig. 2), and in the neighbouring shelf area deeper than 125 m. Because the simulation is located at the top of the shelf break, where the amplitude of internal waves, and therefore their cooling effect at the surface, is maximum, the results at 5 m (Fig. 16a) should be compared to the coolest values in the validation set, which they actually fit. At 50 m (Fig. 16b), the validation data bracket the simulation by about $\pm$ 1^{o}C. This is because instantaneous measurements may show a warmer or cooler temperature depending whether the thermocline is above or below the 50 m level, and these high-frequency oscillations are not explicitly included in the model. The average fit, however, is satisfactory. The fit is also satisfactory at 100 m (Fig. 16c), with a much lesser range of variation in the validation set, except for the period September to November (Julian days 250 to 320). At this time of the year, the thermocline level has deepened to below 100 m, so that high-frequency variations not explicitly expressed in the coupled model outputs also take place at this depth. The comparison of the temperature profiles simulated over the abyssal plain and the top of the shelf break (Fig. 17) shows a surface temperature difference ranging from 0.5^{o}C (in winter) to 3^{o}C on day 210 (late July). The deeper thermocline over the shelf break is also characterized by a much smoother vertical temperature gradient, which tends to be constant in the upper 100 m. The simulated and measured daily-mean depth of isotherms 13.5, 14.5 and 15.5^{o}C are compared at stations P1 (Fig. 18) and P2 (Fig. 19) between Julian days 247 and 287 (6^{th} September to 16^{th} October), 1985 (no measurements are available from P2 between days 258 and 268). Descrepancies between the (whole year) simulation and the measurements are shown in the bottom diagrams of both figures, in the form of root mean square (RMS) profiles. The simulated isotherms show an overall consistency with the observations, but, even though all temperatures are integrated over two M2 tidal periods (24.84 h), the observed isotherms show oscillations of variable amplitude, most pronounced at the time of large spring tides around days 262 and 276 (see Fig. 15). During the comparison period, the isotherm 14.5^{o}C corresponds to the middle of the thermocline and shows the largest observed oscillations. The

deepening of the simulated thermocline from day 275 onwards is initiated by a strong wind stress event (see Fig. 15). The RMS profiles at stations P1 and P2 show maximum values at the thermocline level, i.e. where the effect of high-frequency oscillations not explicitly modelled (see above) is expected to be the largest. They also show a slight increase (from 0.3 to 0.5^{o}C) from about 20 m to the surface, which is most sensitive to meteorologically induced variations. The profiles also show lower values than those obtained over a decade above the abyssal plain by simulating the thermal structure according to the GGL TKE model only. Taking into account the internal mixing thus results in a more accurate simulation. In particular, the high RMS values (ca. 1.20^{o}C) obtained between 30 and 70 m, the depth range most sensitive to the effect of the internal tide, are strongly reduced (to ca. 0.45^{o}C) in the present exercise.
Figure 20 shows two examples of simulated vertical sections along a transect centered at the top of the shelf break (x=0). A well stratified situation is found on day 225 (Fig. 20a), with a thermocline at 50 m along the whole transect, in contrast with the assymmetric temperature distribution at the surface (see below). Day 270 (Fig. 20b) corresponds to a post-spring tide situation (largest tide on day 262) and clearly illustrates the internal diffusive effect, which tends to vertically spread the isotherms within the thermocline, instead of deepening the latter as pure wind-induced mixing would have done. Figure 21 shows the temporal evolution of sea surface temperature along the same transect as in Fig. 20. Internal wave mixing operates for 30 days, beginning on 15 May (day 135), before a significant effect is obtained in terms of heat diffusion near the shelf edge. The distribution of sea surface temperature along the transect is assymmetric. The temperature minimum is found close to the top of the shelf break (x=1 km), rather than at the maximum of tidal forcing (x=-3 km). For the purpose of spatial validation (at the surface), AVHRR scenes of the Bay of Biscay have been selected in the period September-October 1985 (Mazé and Langlois, 1992) for clear chronological series over 2-3 days, covering a neap tide or a spring tide situation. The scenes were inter-calibrated and filtered according to Gohin and Langlois (1993). A mean transect 125 km long and 45 km wide over the central area of cruise ONDINE 85 (Fig. 2, area B) was extracted, yielding an average data set which can be correlated with the modelled temperature. The values were then smoothed with a polynomial filter over 5 points. The area selected is centered over the most persistent cold spot over the shelf break, offering a view of the strongest surface effect of internal waves during the neap-spring alternation. Three series of satellite data are presented on Fig. 22 and

compared to the results of the model: 6-8th September (days 250-252), 17-18th September (days 261-262) and 4-5th October (days 278-279). To alleviate the bias introduced in the comparison by the instantaneous character of satellite measurements (1 AVHRR scene per day for 2-3 days), the mean simulated SST is presented together with the maximum and minimum simulated SST (thin lines). The first situation (6-8th September, Fig. 22a) was just before a spring tide (9th September), with a weak observed gradient (bold line) over the transect. The second situation (Fig. 22b) corresponds to a spring tide and a strong gradient is observed, with a 50-km wide cooler area centered near the north-northeastern shelf edge (x=10 km). In both situations the SST distribution was symmetric over the plain and the shelf, in contrast with the third situation (Fig. 22c), which shows a colder SST over the shelf than over the plain and corresponds to an average tide (following a spring tide). The simulated temperature is in reasonable agreement with the satellite data, and the colder area near the shelf edge is also well reproduced. The RMS difference between the mean simulated SST and the observed data does not exceed 0.5^{o}C, which is also the value obtained at the surface for stations P1 and P2 (see above). The best agreement is observed for the spring tide situation (Fig. 22b), and the less satisfactory one for the early October average tide (Fig. 22c). The reasons for the discrepancy are not entirely clear. Early October is characterized by a strong wind event, from day 275 (2nd October) to day 283. This initiates the deepening of the thermocline (the difference between the maximum and minimum simulated SST is two to three times smaller than previously) and may to some extent affect the accuracy of satellite temperature measurements through their sensitivity to the sea surface state. Another weak point in the simulation is that, near the top of the shelf break, a numerical peak appears because of the lack of advection and the low horizontal resolution. The model shows also its limits when, in the shallower part of the shelf (x $\geq$ 30-40 km, water column height 100-150 m), SST values, except for the spring tide situation, appear to be overestimated. In this area, horizontal or three-dimensional processes and structures, such as instantaneous and residual circulation associated with tidal currents, or micro- to mesoscale turbulence, are likely to be non-negligible, so that one-dimensional vertical modelling may reach there a limit. This interpretation is borne out by the relationship of the discrepancy to the neap spring cycle. When strong tidal currents are present, they tend to inhibit the baroclinic circulation (Linden et al., 1988). On the other hand, when tidal amplitudes are smaller, i.e. when the

discrepancies are larger, the horizontal processes neglected in the model are expected to increase in relative importance with respect to the vertical processes taken into account.

5 Conclusions

The atmosphere-ocean fluxes and the initial conditions are, in this order, the most important sources of errors as regards the one-dimensional mixed layer model. The wind stress was admittedly overestimated by Gaspar et al. (1990) when validating their model. We adjusted the calibration of TKEm to avoid this problem. A better estimation of upper ocean turbulence is obtained when considering the effect of salinity. This was not attempted in the present case, because of the weakness of the actual salinity gradient, but can be achieved with a good estimation of the latent heat flux, or by forcing the model with surface salinity data using an assimilation method. The results relevant to the effect of balancing the annual budgets are more specific to the present study, because attempting such a balance can be justified only at mid-latitudes. A tempting alternative, namely extracting forcing values from a global model, can, however, result in uncertainties whose magnitude will increase in proportion to the coarseness of the calculation grid, and in inverse proportion to the density of associated measurements. In other words, when forcing an upper ocean model with atmospheric fluxes, the quality of the input data has to be assessed before the approximation done in the calculation of ocean turbulence can be evaluated.

The coupling of the GGL model, forced by realistic winds and heat fluxes for 1985, with a - one-dimensional horizontal, two-layer verical - model of non-linear internal waves across the shelf break front in the northern Bay of Biscay produces horizontal and vertical temperature gradients along the simulated transect. This result reflects a variability of mixing regimes along both dimensions of the vertical transect. Because wind mixing is homogeneous along the transect, the heterogeneity in mixing intensity is accounted for by the current shears due to the internal waves. The internal mixing begins to take place when a significant thermocline builds up (mid-May) and develops in summer and autumn when the thermocline deepens and oscillates with an increasing amplitude. As opposed to wind mixing, which causes a deepening of the isotherms and an erosion of the thermocline at its base, the internal mixing tends to vertically spread the isotherms and erode the thermocline at both its upper and lower

boundaries. In terms of SST distribution, the numerical simulation produces a horizontal gradient along the transect which can reach 1.5°C over 35 km. The results are in good agreement with the hydrographic and satellite data in September and October 1985, especially at spring tides and over the continental slope and the abyssal plain. The agreement, however, is less satisfactory at low-amplitude tides over the shallower part of the shelf ($x \geq 40$ km), which may be due to horizontal processes not taken into account in the one-dimensional component of the model. The numerical model has some inherent limitations that preclude it from adequately simulating some of the fine mechanisms of the mixing processes. Most notably, the performance is limited by the approximative representation of the bottom slope and by the non-representation of non-hydrostatic dispersion. The numerical experiments of Gekerma and Zimmermann (1995) showed that the non-linear internal tide manifests itself in a disintegrated form if the parameters of non-hydrostatic and Coriolis dispersion are both sufficiently small in comparison with the parameter of non-linearity. The negative salinity gradient of -0.1 psu in the top 200 m observed over most of the year might be responsible for non-negligible vertical mixing. The high TKEm value, however, has been set to balance this lack of hydrostatic mixing. The one-dimensional component of the model fails to include a formulation for mesoscale circulation and for relatively large-scale eddies which may play a non-negligible role in horizontal mixing and advection. Such eddies are present seasonally in the Bay of Biscay; they can reach a diameter of 100 km and can last several months (Deschamps et al., 1984; Pingree and Le Cann, 1992a, 1992b; Druon, 1995). On a smaller spatial scale, the frontal slope between waters of different density produces a cross-frontal velocity shear which results in the formation of frontal eddies (refs in Le Fèvre, 1986), which also contribute to horizontal advection and mixing. The calculations of Xing and Davies (1997) show that, in the case of an upwelling-favourable wind, the density gradient in the near-bottom region is increased. With a downwelling-favourable wind, the amplitude of the current and of the internal tide motion are significantly reduced due to the change of the density field in the region of internal tidal production. However, our model cannot take account of such wind effects on internal waves because of the omission of horizontal advection. This limitation is because we consider a relatively simplified conceptual framework which does not require too much computing power. Despite the approximation, the main numerical simulation is consistent with the formation of the cooler surface water near the shelf edge as a result of locally generated internal waves

propagating in a non-linear way. The barotropic tidal current towards a continental slope creates a vertical component which leads to a periodic vertical motion of the thermocline. The non-linear oscillations of tidally induced internal waves are the main phenomenon responsible for the seasonal front, and for the interannual SST anomaly, along the shelf break of the Bay of Biscay. Shelf break fronts are present at the edge of many continental margins, and the associated vertical motion and mixing can be expected to play a major role in the high biological productivity (e.g. +25% in the study area, see Druon, 1998) usually encountered in such regions.

Appendix

A The momentum and TKE equations

The host model includes the conservation of momentum which is written in the one-dimensional case:

$$\frac{\partial \bar{u}}{\partial t} = -f\mathbf{k}\bar{u} + \frac{\partial}{\partial z}\left(K_m \frac{\partial \bar{u}}{\partial z}\right)$$

where u is the horizontal velocity of the water; f is the Coriolis partameter; $\mathbf{k}$ is the vertical unit vector; K_m is the eddy diffusivity coefficient for momentum.
Using the same classical concept of eddy diffusivity, the 1-D rate equation of TKE is written:

$$\frac{\partial \bar{e}}{\partial t} = \frac{\partial}{\partial z}\left(K_e \frac{\partial \bar{e}}{\partial z}\right) + \frac{\partial}{\partial z}\left(K_e \frac{\partial \bar{u}}{\partial z}\right) - K_H N^2 - \epsilon$$

where K_e and K_H are the eddy diffusivities for TKE and heat respectively, N is the Brunt-Väisälä or buoyancy frequency, and ϵ is the turbulent dissipation. The usual assumption $K_e = K_H = K_m/P_{rt}$ is made with $P_{rt} = 1$, the turbulent Prandl number (Bougeault and Lacarrère, 1989). As in Gaspar et al.(1990), the eddy diffusivity and the turbulent dissipation are related to TKE according to

$$K_m = c_k l_k (\bar{e})^{1/2}$$
$$\epsilon = c_\epsilon (\bar{e})^{3/2}/l_\epsilon$$

where $c_k = 0.1$ and $c_\epsilon = 0.7$ are the same constants as in Gaspar et al. (1990), l_k and l_ϵ are the mixing and dissipation lengths defined by Bougeault and Lacarrère (1989):

$$l_k = min(l_u, l_d)$$
$$l_\epsilon = (l_u l_d)^{1/2}$$

where l_u and l_d are given at any depth by (Bougeault and André, 1986):

$$\frac{g}{\rho_0}\int_z^{z+l_u} (\bar{\rho}(z) - \bar{\rho}(z'))dz' = \bar{e}(z)$$
$$\frac{g}{\rho_0}\int_z^{z-l_d} (\bar{\rho}(z) - \bar{\rho}(z'))dz' = \bar{e}(z)$$

where $z + l_u$ and $z - l_d$ are limited by the ocean surface and bottom.

B The two-layer characteristics: g' and h_1

The estimation of a two-layer profile is needed to model oscillating internal waves in the present parameterization. The two-layer system is entirely described by three parameters, h_1, T_1 and T_2, the salinity is considered constant, with h_1 the mixed layer depth, T_1 and T_2 the upper and lower layer temperature respectively. The conservation equation of potential energy and internal energy are used. The potential energy of a water column of depth H is written from Lindzen (1990):

$$Ep = \int_0^H \rho g z \, dz \tag{9}$$

which becomes in the two-layer configuration:

$$Ep_2 = \tfrac{1}{2} g \rho_2 \left[H^2 - \alpha_T (T_1 - T_2) h_1^2\right]$$

where $\rho_1 = \rho_2[1 - \alpha_T(T_1 - T_2)]$, and α_T is the heat expansion coefficient. In a discrete representation of dimension N_d, (9) is then written:

$$Ep_{N_d} = \frac{1}{2} g \rho_2 (\Delta z)^2 \sum_{i=1}^{N_d - 1} [1 - \alpha_T (T_i - T_{N_d})](2i - 1) \tag{10}$$

The internal energy of a water column of depth H is written:

$$Ei = \int_0^H \rho \mathcal{C} (T - T_r) \, dz \tag{11}$$

T_r is the reference temperature. In the two-layer system, with the approximation $T_r = T_2$, (11) becomes:

$$Ei_2 = \rho_2 \mathcal{C} (T_1 - T_2)[h_1 - \alpha_T (T_1 - T_2) h_1]$$

In the discrete representation of dimension N_d, (11) is written:

$$Ei_{N_d} = \rho_2 \mathcal{C} \Delta z \sum_{i=1}^{N_d - 1} [1 - \alpha_T (T_i - T_{N_d})](Ti - T_{N_d}) \tag{12}$$

The approximation $T_2 = T_{N_d}$ is made to close the system. The determination of h_1 is then easily performed solving $Ep_2 = Ep_{N_d}$ and $Ei_2 = Ei_{N_d}$, and $g' = g \alpha_T (T_1 - T_2)$. It must be noticed that the principle of total energy conservation is not strictly respected as the kinetic energy is not expressed, and this would need one more equation to close the system. The approximation of T_2 is an underestimation, which induces an overestimation of h_1.

References

Archer, D., 1995. Upper ocean physics as relevant to ecosystem dynamics: a tutorial. Ecological Applications 5, 724-739.

D'Asaro, E. A., 1985. Upper ocean temperature structure, inertial currents, and Richardson numbers observed during strong meteorological forcing. Journal of Physical Oceanography 15, 943-962.

Baines, P.G., 1982. On internal tide generation models. Deep-Sea Research 29, 307-338.

Bougeault, P, André, J.C., 1986. On the stability of the third-order turbulence closure for the modeling of the stratocumulus-topped boundary layer. Journal of Atmospheric Science 43, 1574-1581.

Bougeault, P, Lacarrère, P., 1989. Parameterization of orography-induced turbulence in a meso-beta scale model. Monthly Weather Review 117, 1872-1890.

Davis, R.E., deSzoeke, R., Niiler, P., 1981. Variability in the upper ocean during MILE. Part I. The heat and the momentum balances. Deep-Sea Research 28, 1427-1451.

Deschamps, P.Y., Frouin, R., Crépon, M., 1984. Sea surface temperatures of the coastal zones of France observed by the HCMM satellite. Journal of Geophysical Research 89, 8123-8149.

Dickson, R.R., Gurbutt, P.A., Narayana Pillai, V., 1980. Satellite evidence of enhanced upwelling along the European continental slope. Journal of Physical Oceanography 10, 813-819.

Druon, J.N., 1995. Etat de l'art en couleur de l'océan. Rapport scientifique, Contrat EPSHOM, 118pp.

Druon, J.N., 1998. Modélisation d'écosystèmes pélagiques dans le proche Atlantique : interactions entre les phénomènes physiques et biologiques. Thèse de 3ème cycle de l'Université Paris VI, Océanographie Biologique, 228pp.

Druon, J.N. and J. Le Fèvre, 1999. Sensitivity of a pelagic ecosystem model to variations of process parameter within a realistic range. Journal of Marine Systems, 19, 1-26.

Gargett, A. E., 1984. Vertical eddy diffusivity in the ocean interior. Journal of Marine Research 42, 359-393.

Gargett, A.E., Holloway, G., 1984. Dissipation and diffusion by internal wave breaking. Journal of Marine Research 42, 15-27.

Gaspar, P., Grégoris, Y., Lefevre, J.-M., 1990. A simple eddy kinetic energy model for simulations

of the oceanic vertical mixing: tests at station Papa and long-term upper ocean study site. Journal of Geophysical Research 95, 16,179-16,193.

Gekerma, T., Zimmermann, J.T.F., 1995. Generation of non linear internal tides and solitary waves. Journal of Physical Oceanography, 25, 1081-1094.

Gohin, F., Langlois, G., 1993. Using geostatistics to merge in situ measurements and remotely sensed observation of sea surface temperature. International Journal of Remote Sensing, 14 (1), 9-19.

Heaps, N.S., 1980. A mechanism for local upwelling along the European continental slope. Oceanologica Acta 3, 449-454.

Holligan, P.M., Pingree, R.D., Mardell, G.T., 1985. Oceanic solitons, nutrient pulses and phytoplankton growth. Nature 314, 348-350.

Holloway, P.E., 1994. Observations of internal tide propagation on the Australian North West Shelf. Journal of Physical Oceanography, 24, 1706-1716.

Holloway, P.E., 1996. A numerical model of internal tides with application to the Australian North West Shelf. Journal of Physical Oceanography, 26, 21-37.

Jerlov, N.G., 1968. Optical Oceanography. Elsevier, 194pp.

Johnson, J.A., Nurser, A.J.G., 1983. A model of secondary upwelling over the shelf break. Geophysical and Astrophysical Fluid Dynamics 23, 301-320.

Johnson, J.A., Nurse, A.J.G., 1984. A model of secondary upwelling over the shelf break. II. Geophysical and Astrophysical Fluid Dynamics 28, 161-170.

Large, W.G., McWilliams, J.C., Niiler, P.P., 1986. Upper ocean thermal response to strong autumnal forcing of the northeast Pacific. Journal of Physical Oceanography 16, 1524-1550

Le Cann, B., Cabillic, J., 1979. Contribution à l'étude de la structure hydrologique et hydrodynamique sur le plateau continental sud Bretagne. Rapport de Diplôme d'Etudes Approfondies, Université de Bretagne Occidentale, Brest.

Le Fèvre, J., 1986. Aspects of the biology of frontal systems. Advances in Marine Biology 23, 163-299.

Le Fèvre, J., Frontier, S., 1988. Influence of temporal characteristics of physical phenomena on plankton dynamics, as shown by north-west European marine ecosystems. In: Rothschild B.J. (Ed.). Toward a Theory of Biological-Physical Interactions in the World Ocean. Kluwer Academic Publishers, Dordrecht, 245-272.

Le Tareau, J.-Y., Mazé, R., 1996. On barotropic and baroclinic tides over an arbitrary sloping topography. Annales Geophysicae 14, 961-975.

Linden, T.S., Simpson, J.E., 1988. Modulated mixing and frontogenesis in shallow seas ans estuaries. Continental Shelf Research 8, 1107-1127.

Lindzen, R.S., 1990. Dynamics in atmospheric physics. Cambridge University Press, 310pp.

Marchal, O., Monfray, P., Bates, N.R., 1996. Spring-summer imbalanced dissolved inorganic carbon in the mixed layer of the north western Sargasso sea. Tellus, 48, 115-134.

Mazé, R., 1980. Formation d'ondes internes stationnaires sur un talus continental: application au Golfe de Gascogne. Annales hydrographiques (754), 45-58.

Mazé, R., 1987. Generation and propagation of non-linear internal waves induced by the tide over a continental slope. Continental Shelf Research 7, 1079-1104.

Mazé, R., Camus, Y., Le Tareau, J.Y., 1986. Formation de gradients thermiques à la surface de l'océan, au-dessus d'un talus, par interaction entre les ondes internes et le mélange dû au vent. Journal du Conseil International pour l'Exploration de la Mer 42, 221-240.

Mazé, R., Langlois, G., 1992. Modélisation de l'évolution d'une couche marine superficielle: simulation de la formation d'un front thermique de marée au dessus d'un talus. Rapport Scientifique. Contrat EPSHOM No 4-91, 41pp.

Mitchell J.F.B., Senior, C.A., Ingram, J.W., 1989. CO2 and climate: a missing feeback? Nature 341, 132-134.

New, A.L., Pingree, R.D., 1990. Evidence for internal tidal mixing near the shelf break in the Bay of Biscay. Deep-Sea Research 37, 1783-1803.

Parsons, T. R., Takahashi, M., Hargrave, B., 1984. Biological oceanographic processes. Pergamon Press, Oxford, England.

Paulson, C.A., Simpson, J.J. 1977. Irradiance measurements in the upper ocean. Journal of Physical Oceanography 7, 952-956.

Peixoto, J.P., Oort, A.H., 1992. Physics of climate. American Institute of Physics, New-York, USA.

Pineda, J., 1991. Predictable upwelling and the shoreward transport of planktonic larvae by internal tidal bores. Science 253, 548-551.

Pingree, R.D., 1978. Cyclonic eddies and cross-frontal mixing. Journal of the Marine Biological Association of the United Kingdom 58, 955-963.

Pingree, R.D., Mardell, G.T., 1981. Slope turbulence, internal waves and phytoplankton growth at the Celtic Sea shelf-break. Philosophical Transactions of the Royal Society of London A 302, 663-682.

Pingree, R.D., Griffiths, D.K., Mardell, G.T., 1984. The structure of the internal tide at the Celtic Sea shelf break. Journal of the Marine Biological Association of the United Kingdom 64, 99-113.

Pingree, R.D., Le Cann, B. 1992a. Three anticyclonic slope water oceanic eddies (Swoddies. in the southern Bay of Biscay in 1990. Deep Sea Research 39, 1147-1175.

Pingree, R.D., Le Cann, B., 1992b. Anticyclonic Eddy X91 in the southern Bay of Biscay, May 1991 to February 1992. Journal of Geophysical Research 97, 14353-14367.

Podestà, G., Esaias, W., 1988. Satellite-derived phytoplankton pigment concentrations along the shelf break off Argentina 1979-1980. Eos, 69, 1144 (abstract).

Pollard, R.T., Rhines, P.B., Thompson, R.O.R.Y., 1973. The deepening of the wind-mixed layer. Geophysical Fluid Dynamics 3, 381-404.

Pondaven, P., Ruiz-Pino, D. , Druon, J.N., Fravalo, C., Tréguer, P., 1999. Factors controlling silicon and nitrogen biogeochemical cycles in high nutrient, low chlorophyll systems (the Southern Ocean and the North Pacific): Comparison with a mesotrophic. Deep-Sea Research I, 46 (11), 1923-1968.

Pondaven, P., Ruiz-Pino, D. , Fravalo, C., Tréguer, P., Jeandel, C., in press. Interannual variability of silicon and nitrogen cycles at the time series station KERFIX between 1990 and 1995 - A one-dimensional modelling study. Deep-Sea Research I.

Price, J.F., Weller, R.A., Pinkle, R., 1986. Diurnal cycling: observations and models of the upper ocean response to diurnal heating, cooling and wind mixing. Journal of Geophysical Research 91, 8411-8427.

Rodi, W., 1993. Turbulence models and their applications inn hydraulics. A state-of-the art review. A.A. Balkema Publishers, Rotterdam.

Sandström, H., Elliott, J.A., 1984. Internal tides and solitons on the Scotian shelf: a nutrient pump at work. Journal of Geophysical Research 89, 6415-6426.

Seager, R., Zebiak, S. E., Cane, M.A., 1988. A model of the tropical pacific sea surface temperature climatology. Journal of Geophysical Research 93, 1265-1280.

Shea, R.E., Broenkow, W.W., 1982. The role of internal tides in the nutrient enrichment of

Monterey Bay, California. Estuarine, Coastal and Shelf Science 15, 57-66.

Turner, J.S., 1981. Small scale mixing processes. Evolution of Physical Oceanography, Ed. Warren B. and Wunsch K., MIT Press, Cambridge.

Weare, B.C., Strub, P.T., Samuel, M.D., 1981. Annual mean surface heat fluxes in the tropical Pacific Ocean. Journal of Physical Oceanography 11, 705-717.

Wigley, T.M.L., 1989. Possible climate change due to SO_2– derived cloud condensation nuclei. Nature 339, 365-367.

Xing, J., Davies, A.M., 1996. Processes influencing the internal tide, its higher harmonics and tidally induced mixing on the Malin-Hebrides shelf. Progress in Oceanography, 38, 155-204.

Xing, J., Davies, A.M., 1997. The influence of wind effects upon internal tides in the shelf edge regions. Journal of Physical Oceanography, 27, 2100-2125.

Xing, J., Davies, A.M., 1998a. A three dimensional model of internal tides in the Malin-Hebrides shelf and shelf edge. Journal of Geophysical Research, 103, 27,821-27,847.

Xing, J., Davies, A.M., 1998b. Application of a range of turbulence energy models to the computation of the internal tide. International Journal of Numerical Methods in Fluids, 26, 1055-1084.

Figure legends

Fig. 1 . Annual heat imbalance from 1985 to 1994 at the point 47°N, 6°W (ECWMF fluxes, Météo France).

Fig. 2 . Location of measurement stations used for the validation from 1985 to 1994 (hatched area), and location of the extraction area for the validation of the combined internal wave model (see next section) : (A) the selected stations used for the Fig. 16 (non-hatched zone), stations P1 and P2 (see Figs. 18 and 19), and (B) the AVHRR scenes (see Fig. 22): B1 (46° 55 N ; 6° 40 W), B2 (47° 53 N ; 5° 50 W), B3 (46° 42 N ; 6° 10 W).

Fig. 3 . Simulated (—) and measured (+) (CMO/SHOM) temperature at 5 m from 1985 to 1994 using, (a) balanced annual heat budgets, and (b), the ECWMF original heat fluxes: results of the GGL model.

Fig. 4. Simulated (—) and measured (+) (CMO/SHOM) temperature at 50 m from 1985 to 1994 using, (a) balanced annual heat budgets, and (b), the ECWMF original heat fluxes: results of the GGL model.

Fig. 5. Simulated (—) and measured (+) (CMO/SHOM) temperature at 120 m from 1985 to 1994 using, (a) balanced annual heat budgets, and (b), the ECWMF original heat fluxes: results of the GGL model.

Fig. 6. Monthly mean surface temperature difference (simulation - measurement) from 1985 to 1994.

Fig. 7. Annual root mean square (RMS) profiles of the difference between the modelled temperature (GGL model) and the in situ measurements using balanced annual heat budgets. The decadal RMS profile (dots) is repeated on each annual result, and is compared with the case of imbalanced annual heat budgets (circles).

Fig. 8. Observed and calculated temperature at 5 m, temporal and spatial distribution of the measurement stations in 1988 (SHOM). The continuous line indicates the isobath 200 m.

Fig. 9. Observed and calculated temperature at 5 m, temporal and spatial distribution of the measurement stations in 1994 (SHOM). The continuous line indicates the isobath 200 m.

Fig. 10. Isolines of $\log(10^{5} K_h)$, with K_h in square meters per second for 1985 in the North-East Atlantic (46° 30'N, 6°W). Three-day mean values of K_h are used to draw this figure, as in Gaspar et al. (1990, see Fig. 3).

Fig. 11 . Scheme of the coupling of the 1-D kinetic energy model and the two-layer internal wave model (see text for the definitions).

Fig. 12 . Configuration of the system abyssal plain-shelf break-continental shelf.

Fig. 13 . Amplitude of the current normal to the shelf break created by the wave M2.

Fig. 14 . Amplitude of the tidal forcing on the continental shelf break created by the wave M2.

Fig. 15 . Wind stress at 47°N, 6°W (Météo-France) and sea surface elevation (tidal oscillations of M2 and S2) at the top of the shelf break in 1985 (partial).

Fig. 16 . Comparison of calculated temperatures at the top of the shelf and instantaneous measurements of stations located at less than 50 km of the shelf top and which its lead do not excess 125 m inside the study area 46-48°N, 5-8°W (see the non-hatched area of square (A), Fig. 2). (a) Temperature at 5 m, (b) Temperature at 50 m, (c) Temperature at 100 m.

Fig. 17 . Monthly evolution of the temperature profile from day 150 (May 29^{th}) to day 270 (September 26^{th}), (a) above the abyssal plain (X=-100km), and (b) at the top of the shelf break.

Fig. 18 . (a) Measurements of the isotherms 13.5 14.5 and 15.5°C at 5 km in-shore of the shelf top during ONDINE-85 (-+-) (station P1, CMO/SHOM, September 6^{th}-October 16^{th} 1985), and the corresponding calculated isotherms (—): results of the combined models. (b) Root mean square of the temperature difference between the model and the measurements for the station P1 for the same period, and comparison with the decenal RMS values obtained in the area out of the internal wave influence (X X X) (see Fig. 7).

Fig. 19 . (a) Measurements of the isotherms 13.5 14.5 and 15.5°C at 5 km in-shore of the shelf top during ONDINE-85 (-+-) (station P2, CMO/SHOM, September 6^{th}-October 16^{th} 1985), and the corresponding calculated isotherms (—): results of the combined models. (b) Root mean square of the temperature difference between the model and the measurements for the station P2 for the same period, and comparison with the decenal RMS values obtained in the area out of the internal wave influence (X X X) (see Fig. 7).

Fig. 20 . Spatial distribution of the calculated temperature at the vicinity of the top of the shelf break, (a) at day 225 (August 15^{th}), (b) at day 270 (September 27^{th}): results of the combined models.

Fig. 21 . Temporal evolution of the calculated sea surface temperature (SST) along a transect at the vicinity of the top of the shelf break (X=0 km): (a) from day 150 to day 225, (b) from day 255 to day 285: results of the combined models.

Fig. 22 . Simulated and measured SST along a mean transect normal to the slope of the shelf break. The top of the shelf break corresponds to X = 0. The thin continuous line corresponds to the mean simulated SST over the comparison period, and the correspondant minimum and maximum simulated SST. The wide continuous line represents the observed SST extracted from AVHRR data (see text): (a) September 6^{th}, 7^{th} and 8^{th} 1985 (days 250-252, neap tide), (b) September 17^{th} and 18^{th} 1985 (days 261-262, spring tide), (c) October 4^{th} and 5^{th} 1985 (days 278-279, mean tide).

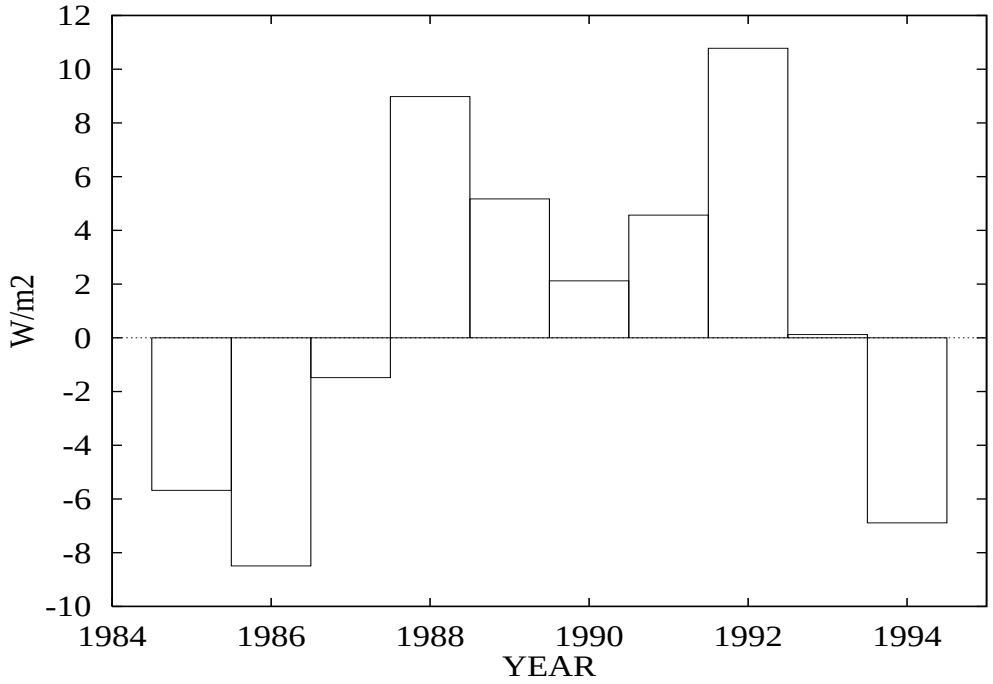

Figure 1:

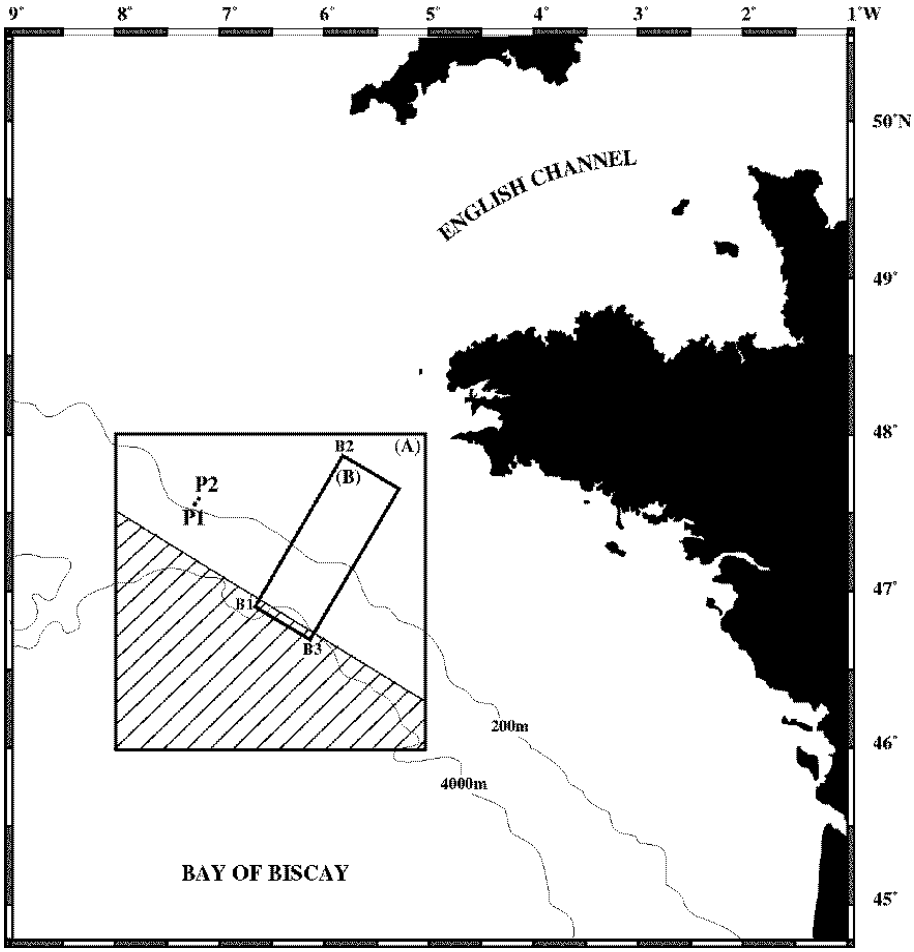
9°
8°
7°
6°
5°
4°
3°
2°
1°W
50°N
49°
48°
47°
46°
45°
ENGLISH CHANNEL
B2
(A)
(B)
P2
P1
B1
B3
200m
4000m
BAY OF BISCAY

Figure 2:

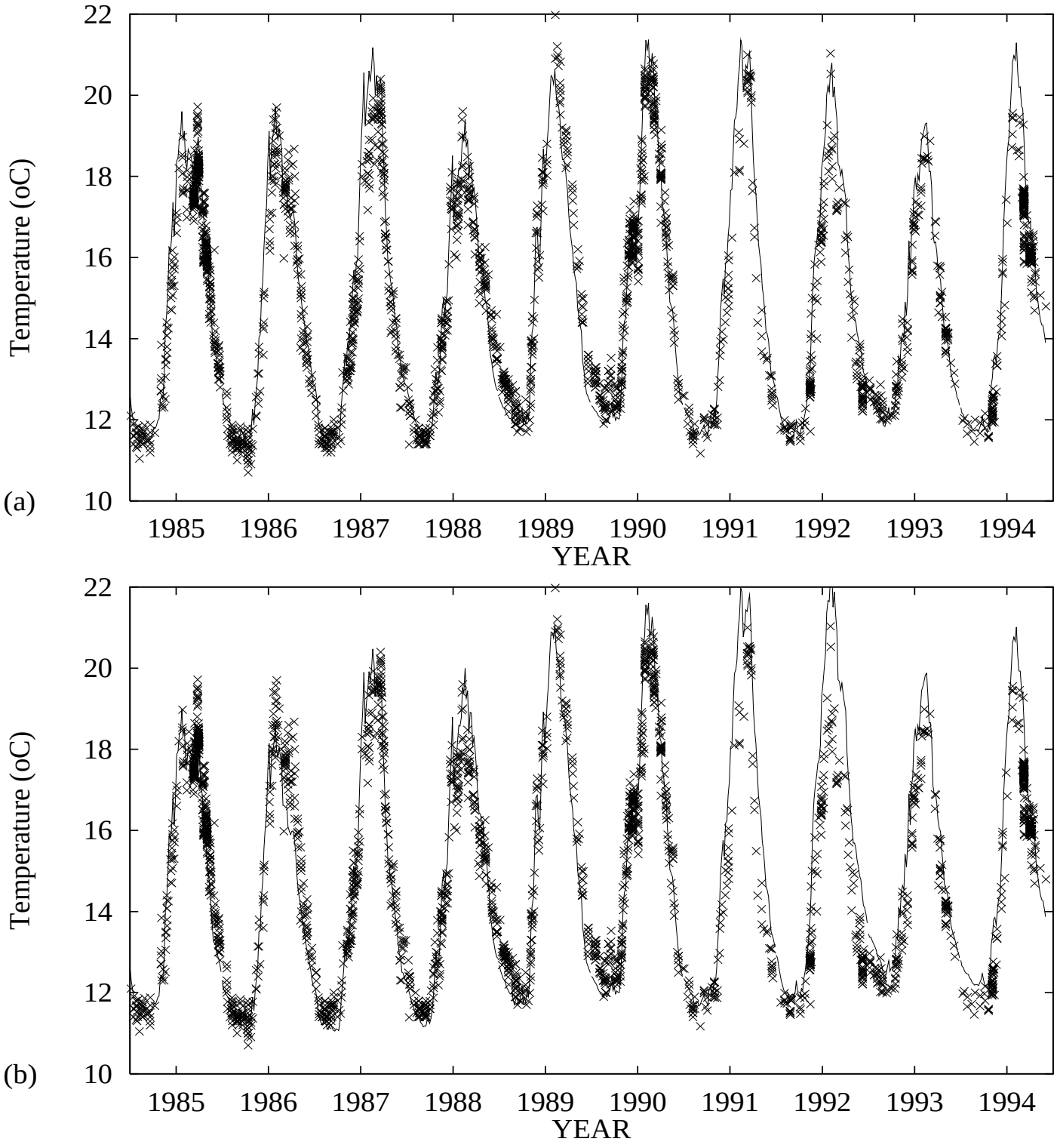
(a)
Temperature (oC)
22
20
18
16
14
12
10
1985
1986
1987
1988
1989
1990
1991
1992
1993
1994
YEAR
(b)
Temperature (oC)
22
20
18
16
14
12
10
1985
1986
1987
1988
1989
1990
1991
1992
1993
1994
YEAR

Figure 3:

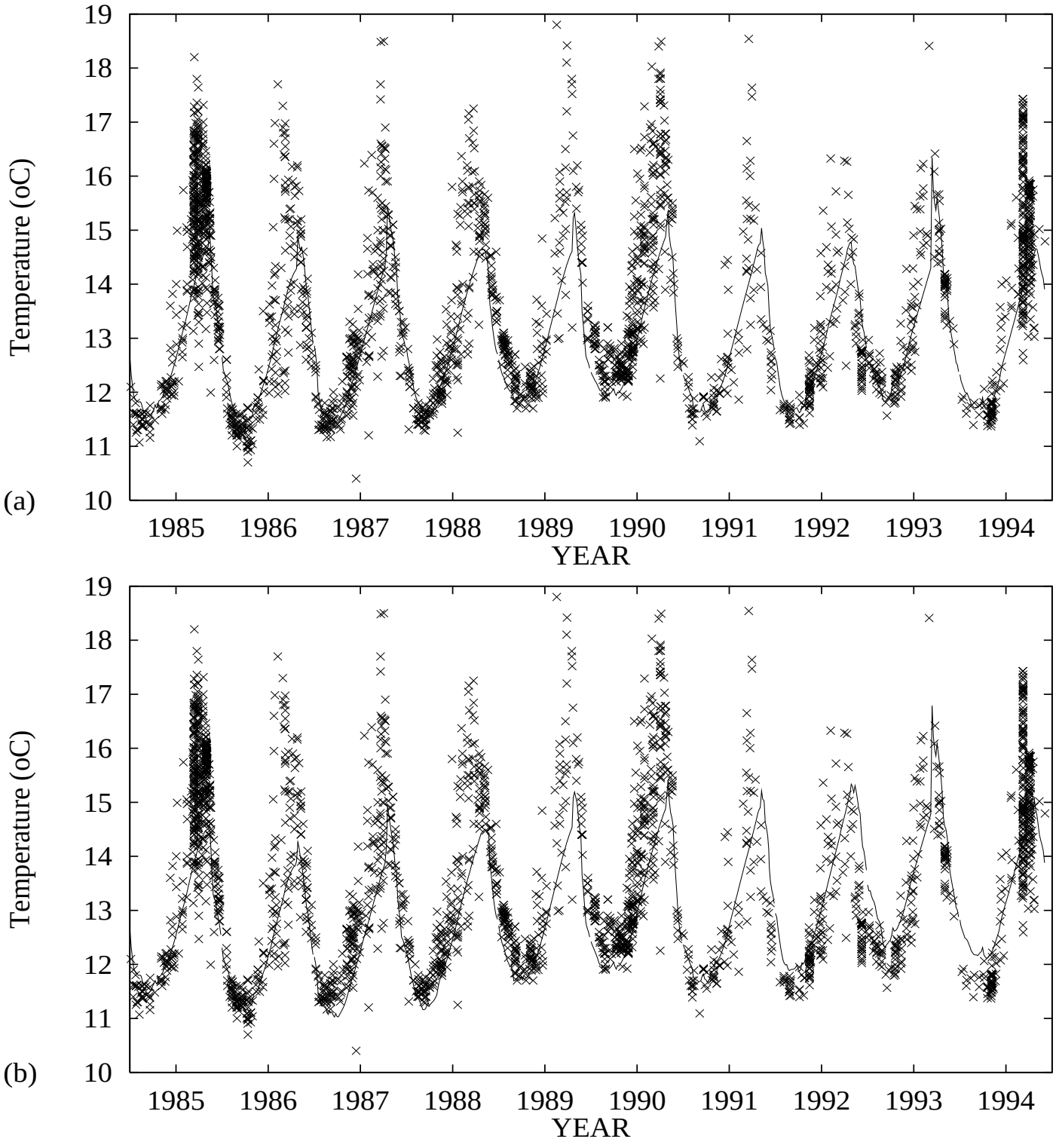
(a)
Temperature (oC)
19
18
17
16
15
14
13
12
11
10
1985
1986
1987
1988
1989
1990
1991
1992
1993
1994
YEAR
(b)
Temperature (oC)
19
18
17
16
15
14
13
12
11
10
1985
1986
1987
1988
1989
1990
1991
1992
1993
1994
YEAR

Figure 4:

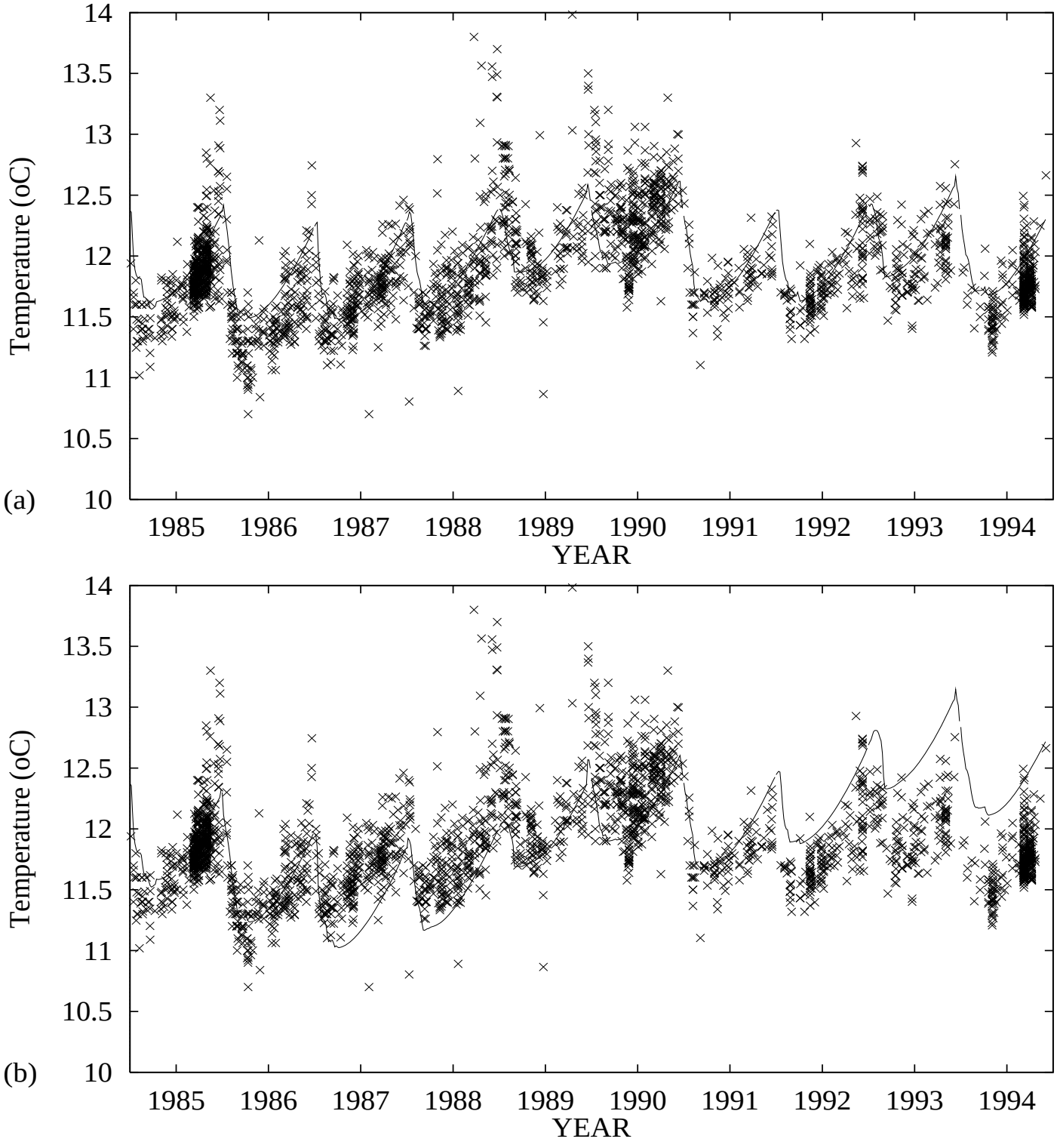
(a)
Temperature (oC)
14
13.5
13
12.5
12
11.5
11
10.5
10
1985
1986
1987
1988
1989
1990
1991
1992
1993
1994
YEAR
(b)
Temperature (oC)
14
13.5
13
12.5
12
11.5
11
10.5
10
1985
1986
1987
1988
1989
1990
1991
1992
1993
1994
YEAR

Figure 5:

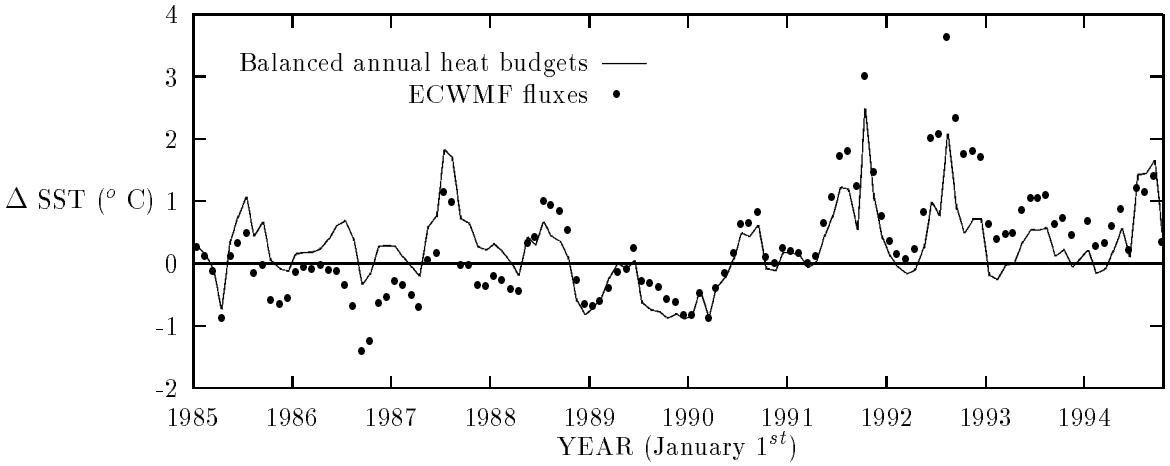
Balanced annual heat budgets
ECWMF fluxes
Δ SST (° C)
4
3
2
1
0
-1
-2
1985
1986
1987
1988
1989
1990
1991
1992
1993
1994
YEAR (January 1st)

Figure 6:

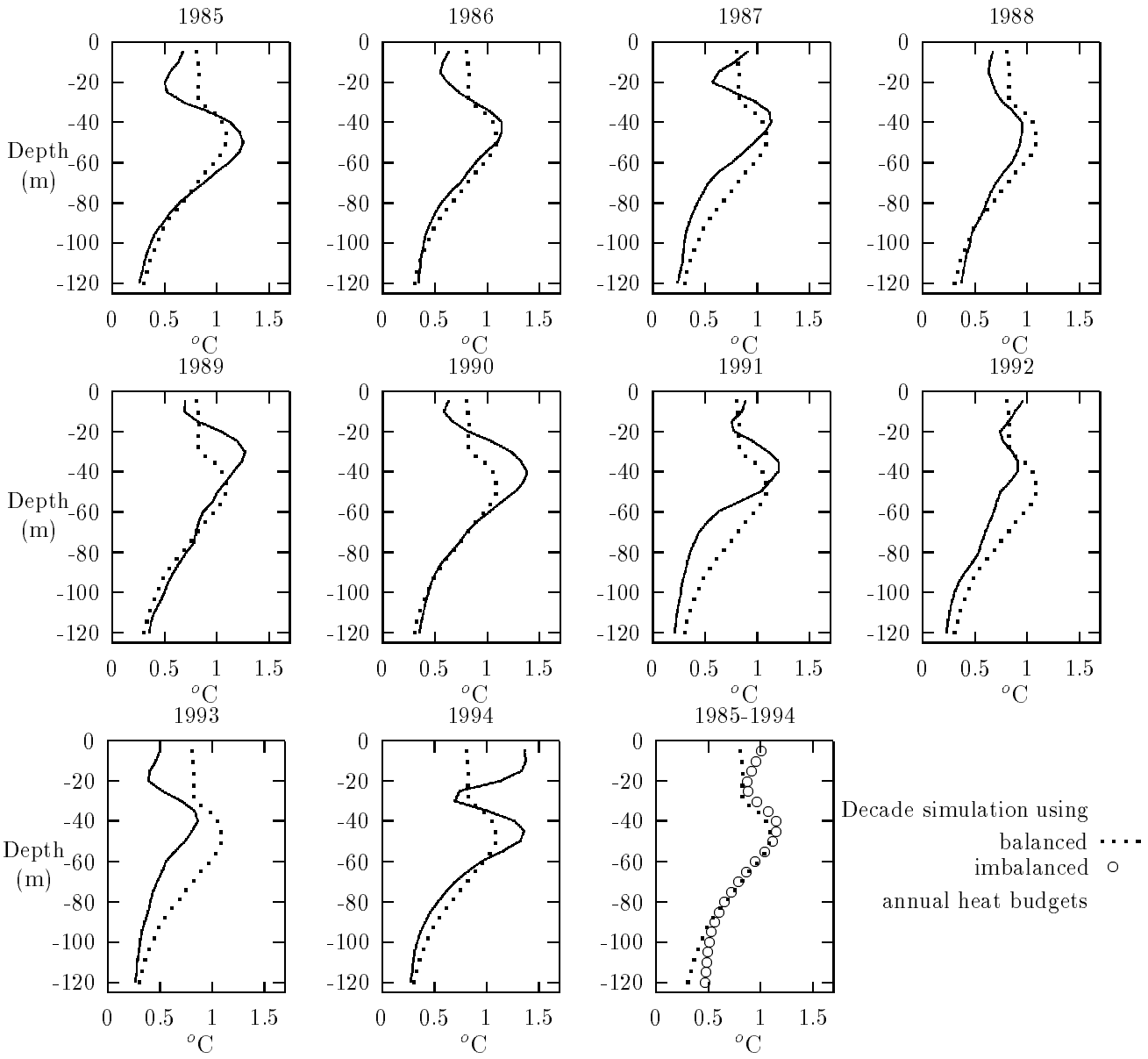
1985
1986
1987
1988
1989
1990
1991
1992
1993
1994
1985-1994
Depth (m)
0
-20
-40
-60
-80
-100
-120
0 0.5 1 1.5
°C
Decade simulation using
balanced
imbalanced
annual heat budgets

Figure 7:

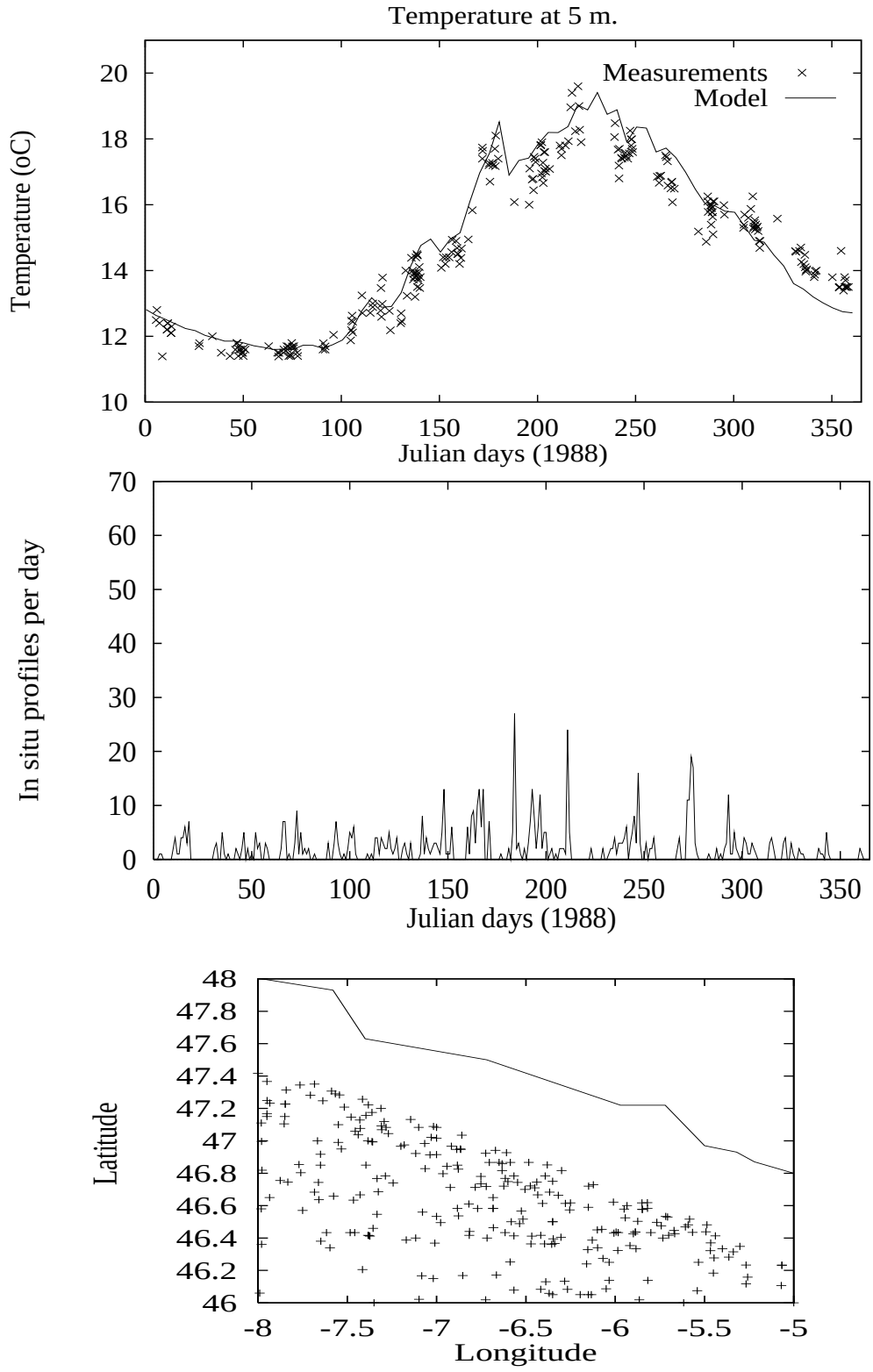
Temperature at 5 m.
Measurements
Model
Temperature (oC)
Julian days (1988)
In situ profiles per day
Julian days (1988)
Latitude
Longitude

Figure 8:

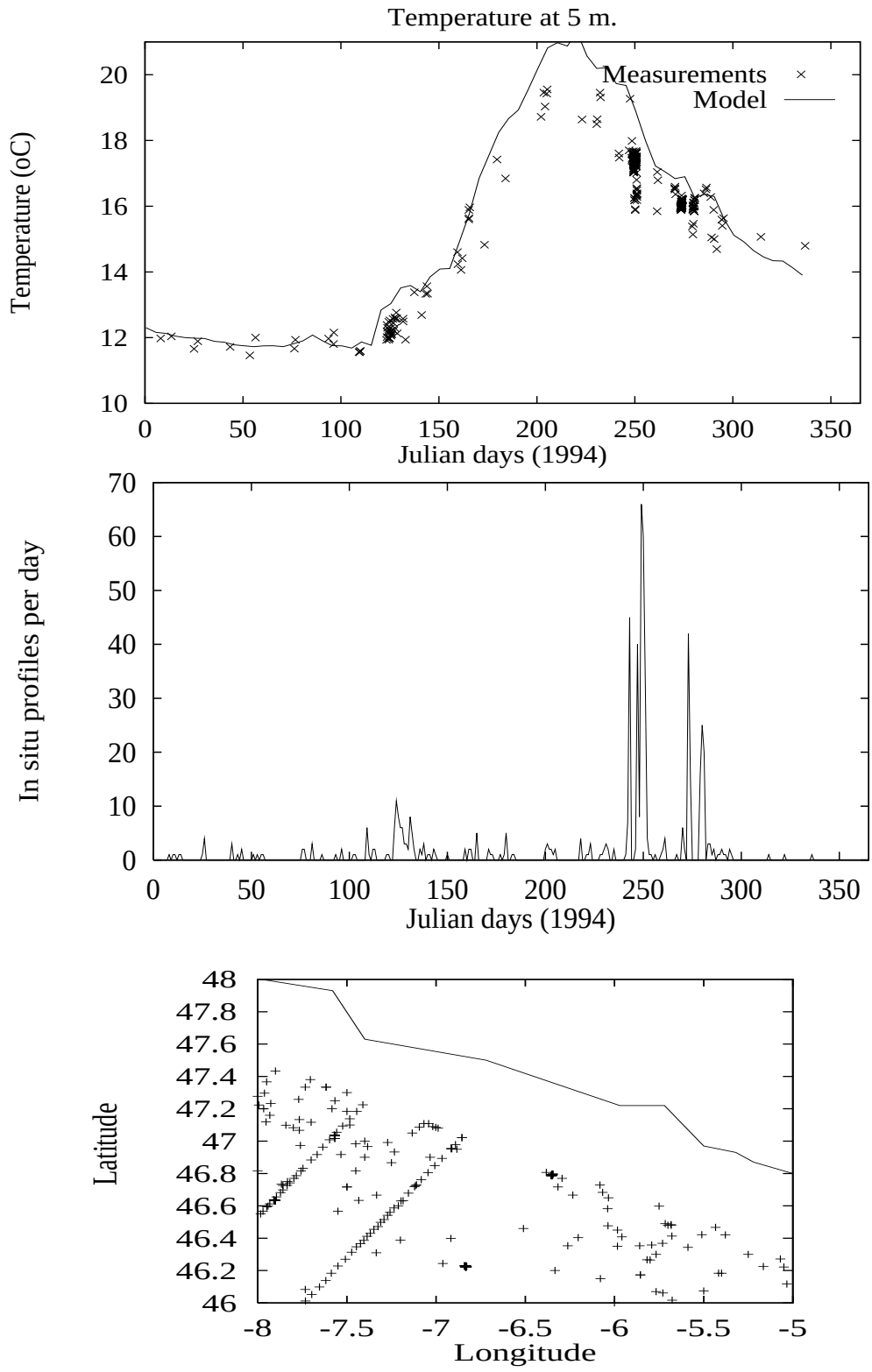
Temperature at 5 m.
Measurements
Model
Temperature (oC)
Julian days (1994)
In situ profiles per day
Julian days (1994)
Latitude
Longitude

Figure 9:

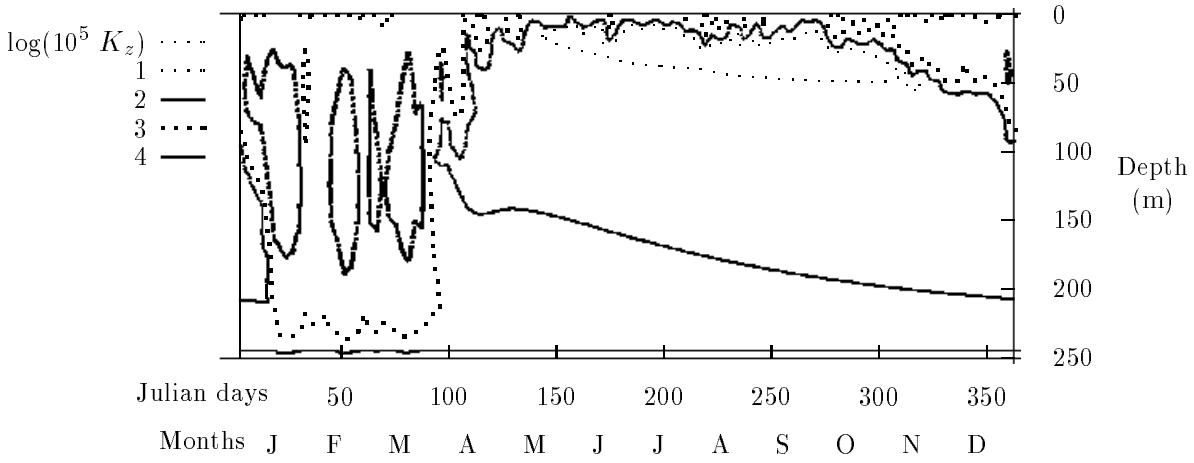
log(10^5 K_z)
1
2
3
4
0
50
100
150
200
250
Depth
(m)
Julian days
50
100
150
200
250
300
350
Months
J
F
M
A
M
J
J
A
S
O
N
D

Figure 10:

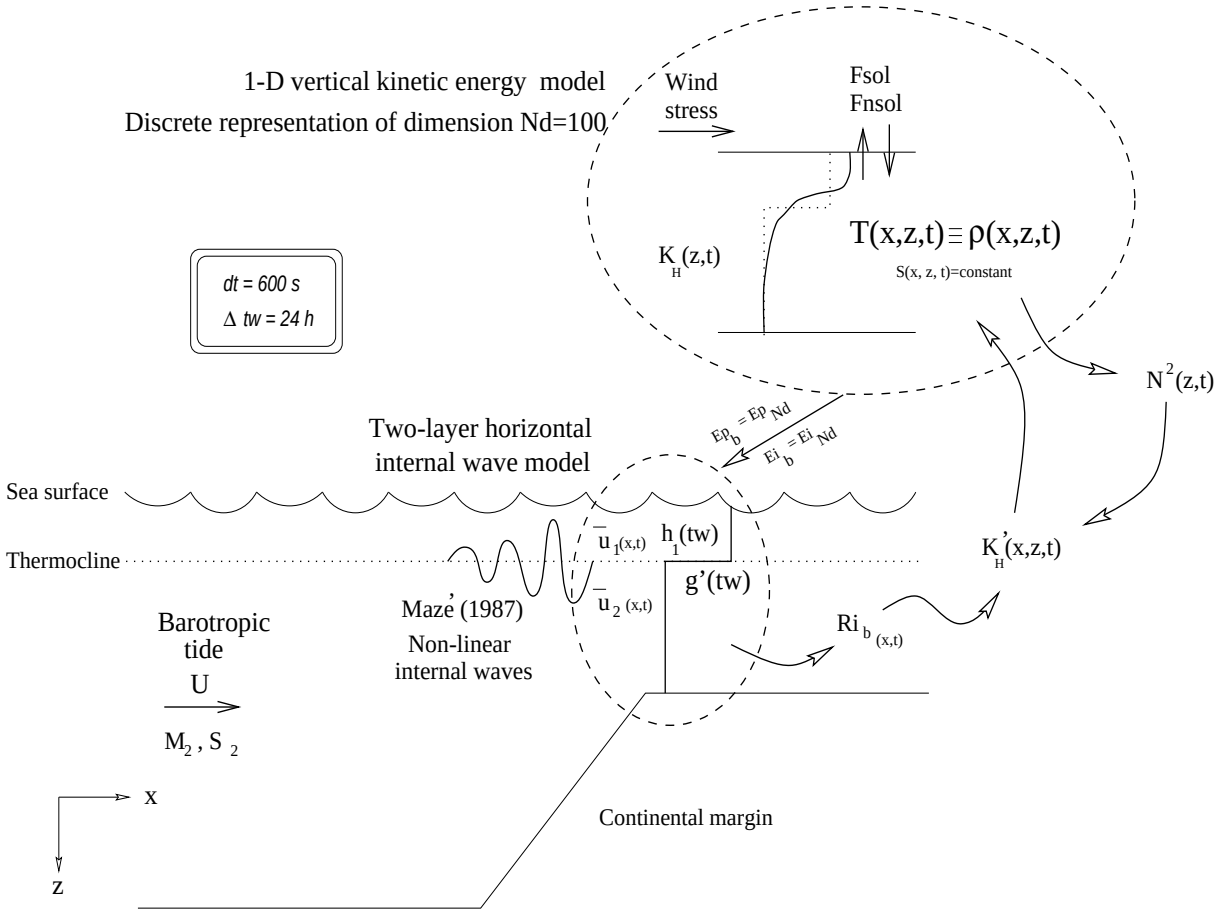
1-D vertical kinetic energy model
Discrete representation of dimension Nd=100
Wind stress
Fsol
Fnsol
K H (z,t)
T(x,z,t) ≡ ρ(x,z,t)
S(x, z, t)=constant
dt = 600 s
Δ tw = 24 h
N 2 (z,t)
Two-layer horizontal internal wave model
Ep b = Ep Nd
Ei b = Ei Nd
Sea surface
Thermocline
u 1(x,t)
h 1(tw)
g'(tw)
u 2 (x,t)
K H'(x,z,t)
Ri b (x,t)
Maze' (1987)
Non-linear internal waves
Barotropic tide
U
M2 , S 2
x
z
Continental margin

Figure 11:

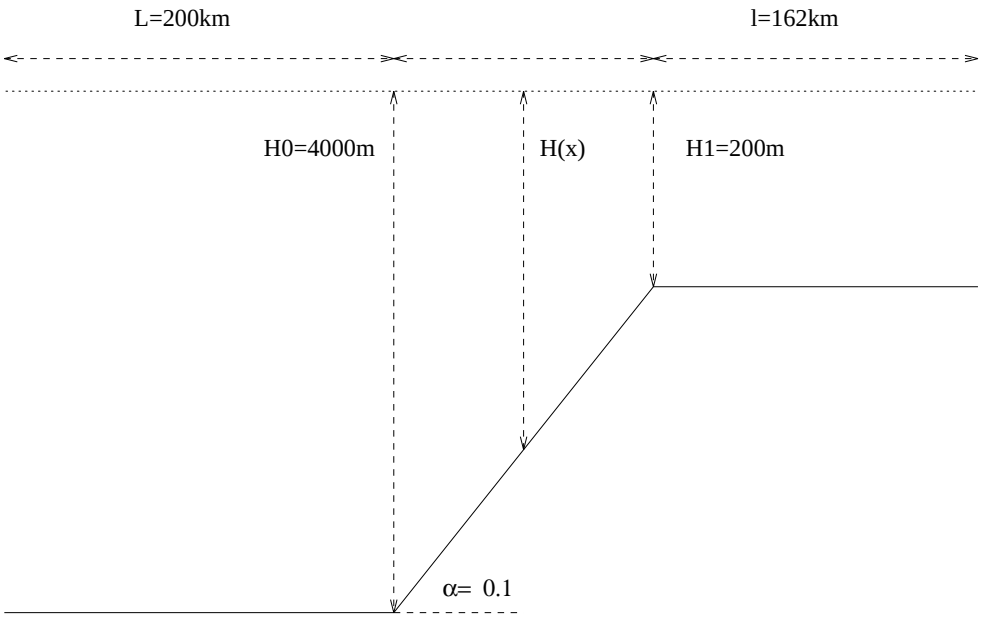

Figure 12:

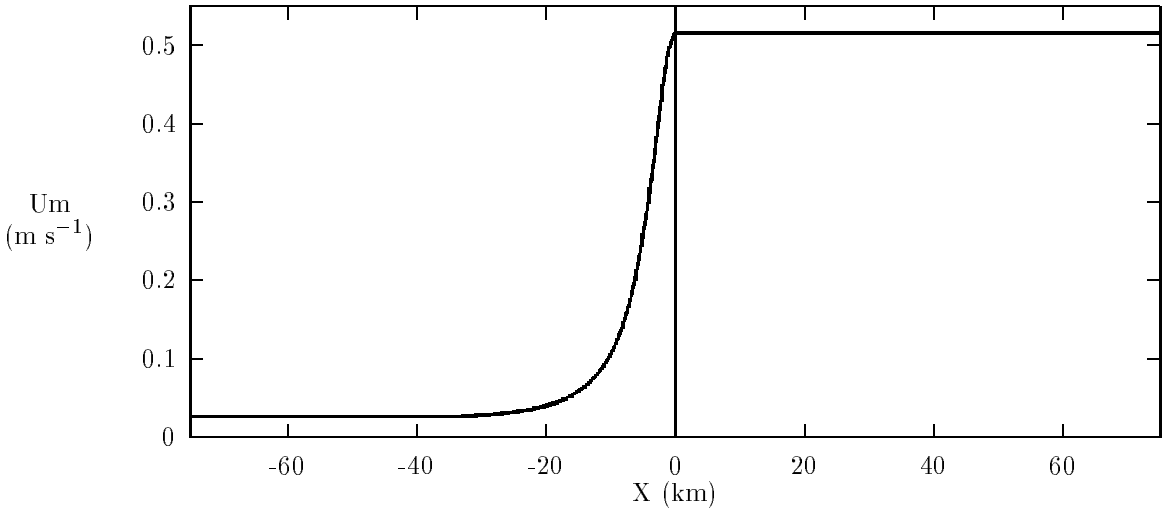

Figure 13:

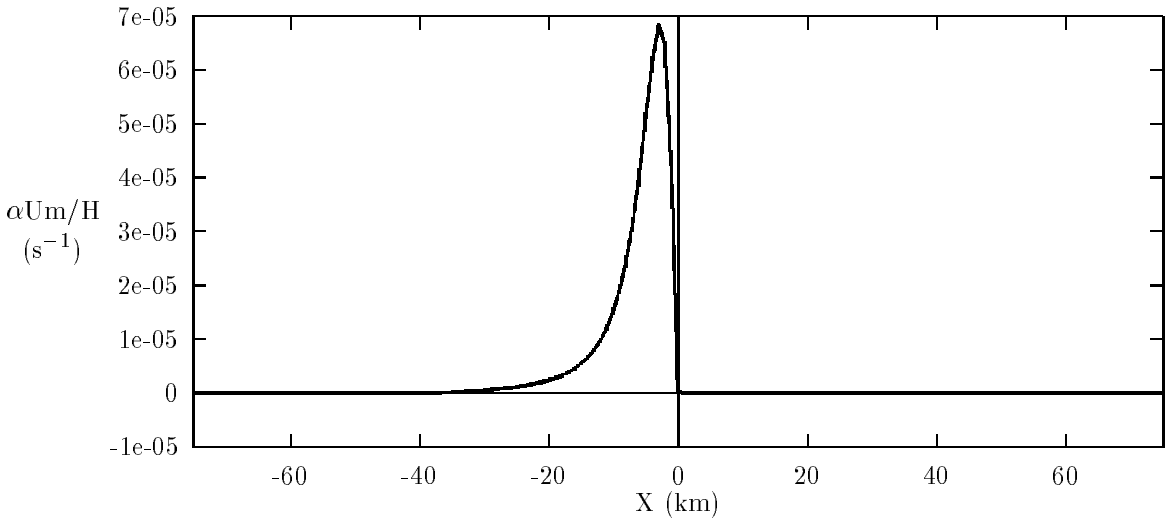
7e-05
6e-05
5e-05
4e-05
3e-05
2e-05
1e-05
0
-1e-05
αUm/H
(s^{-1})
-60
-40
-20
0
20
40
60
X (km)

Figure 14:

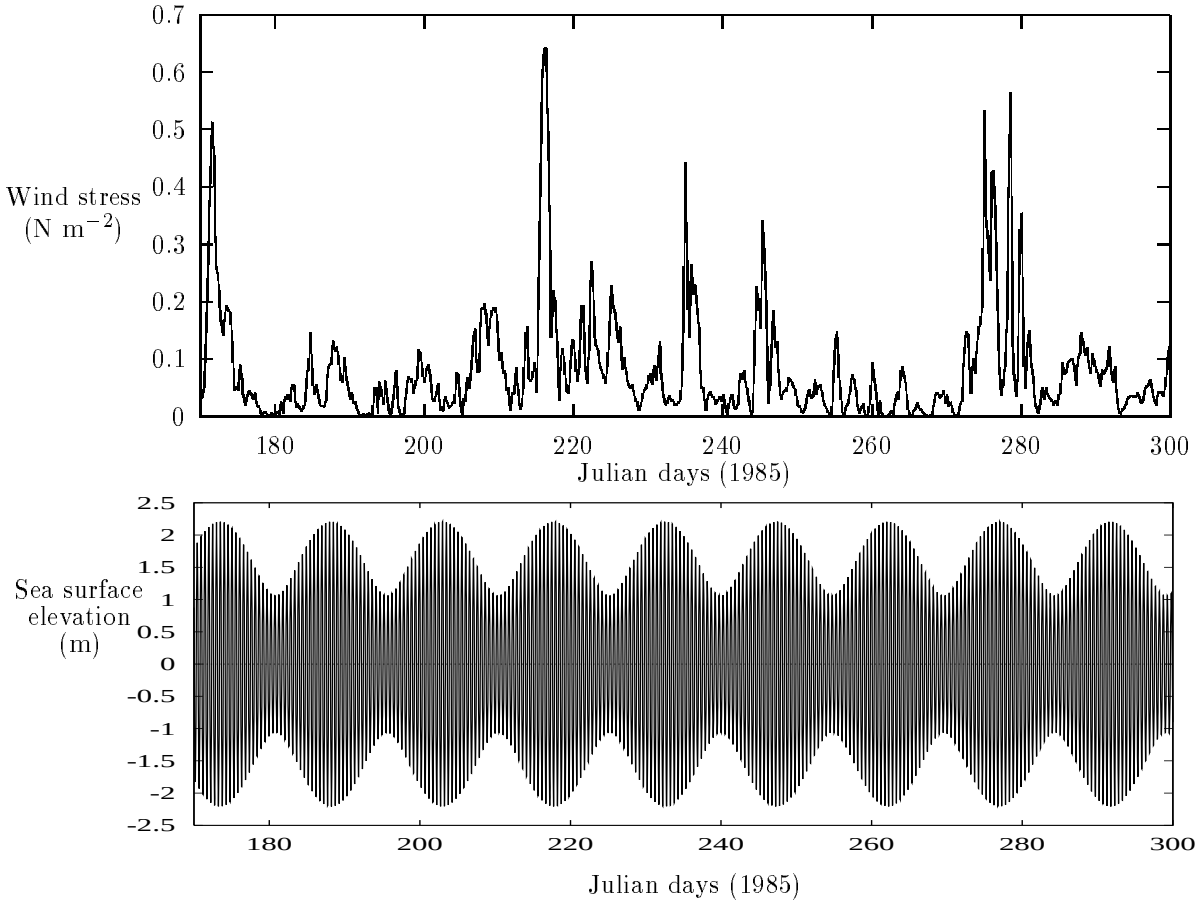
Wind stress
(N m^{-2})
0.7
0.6
0.5
0.4
0.3
0.2
0.1
0
180
200
220
240
260
280
300
Julian days (1985)
Sea surface
elevation
(m)
2.5
2
1.5
1
0.5
0
-0.5
-1
-1.5
-2
-2.5
180
200
220
240
260
280
300
Julian days (1985)

Figure 15:

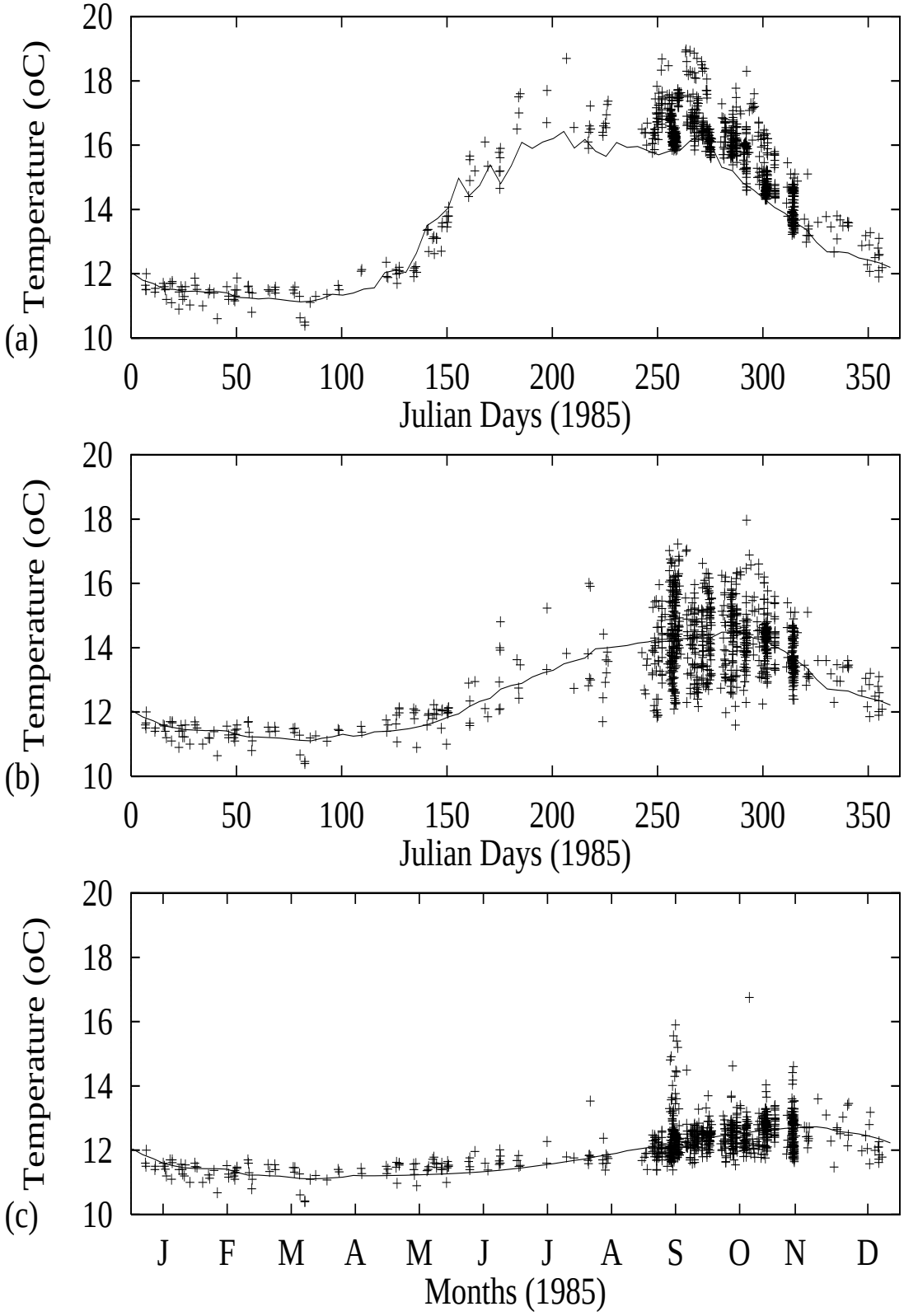
(a)
Temperature (oC)
20
18
16
14
12
10
0
50
100
150
200
250
300
350
Julian Days (1985)
(b)
Temperature (oC)
20
18
16
14
12
10
0
50
100
150
200
250
300
350
Julian Days (1985)
(c)
Temperature (oC)
20
18
16
14
12
10
J
F
M
A
M
J
J
A
S
O
N
D
Months (1985)

Figure 16:

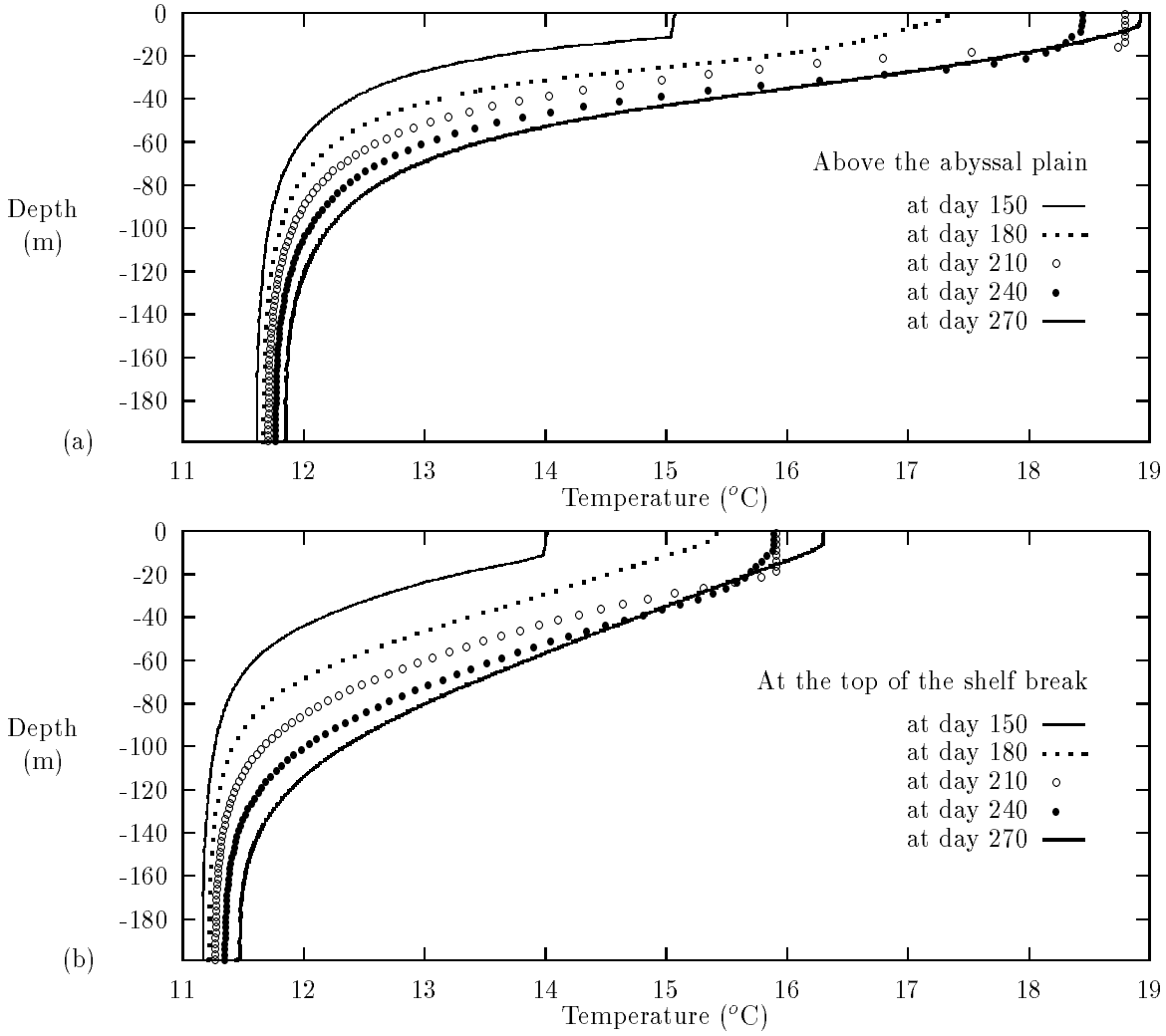
Depth
(m)
0
-20
-40
-60
-80
-100
-120
-140
-160
-180
Above the abyssal plain
at day 150
at day 180
at day 210
at day 240
at day 270
(a)
11
12
13
14
15
16
17
18
19
Temperature (^{o}C)
Depth
(m)
At the top of the shelf break
at day 150
at day 180
at day 210
at day 240
at day 270
(b)
Temperature (^{o}C)

Figure 17:

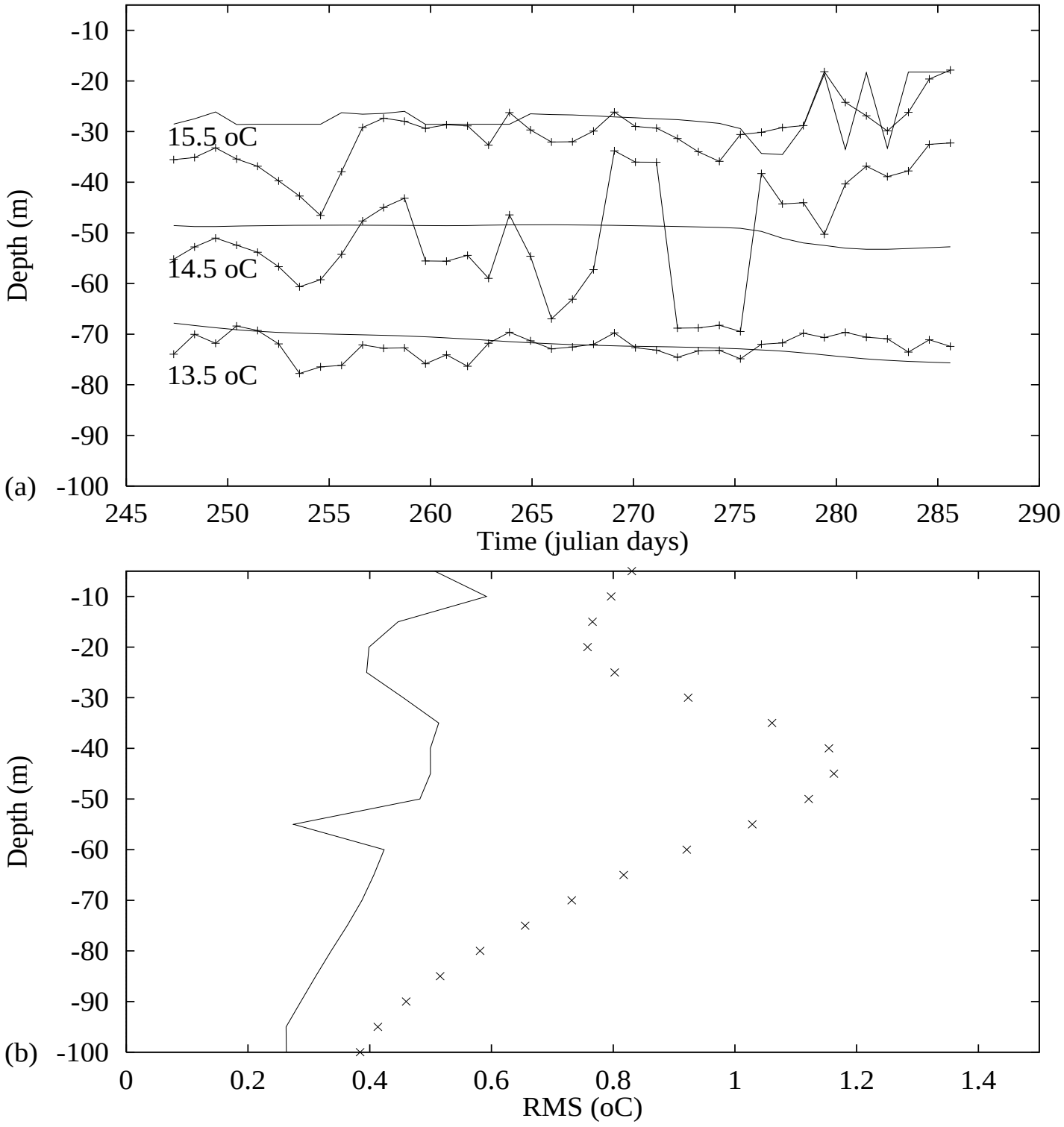
(a)
Depth (m)
-10
-20
-30
-40
-50
-60
-70
-80
-90
-100
15.5 oC
14.5 oC
13.5 oC
245
250
255
260
265
270
275
280
285
290
Time (julian days)
(b)
Depth (m)
-10
-20
-30
-40
-50
-60
-70
-80
-90
-100
0
0.2
0.4
0.6
0.8
1
1.2
1.4
RMS (oC)

Figure 18:

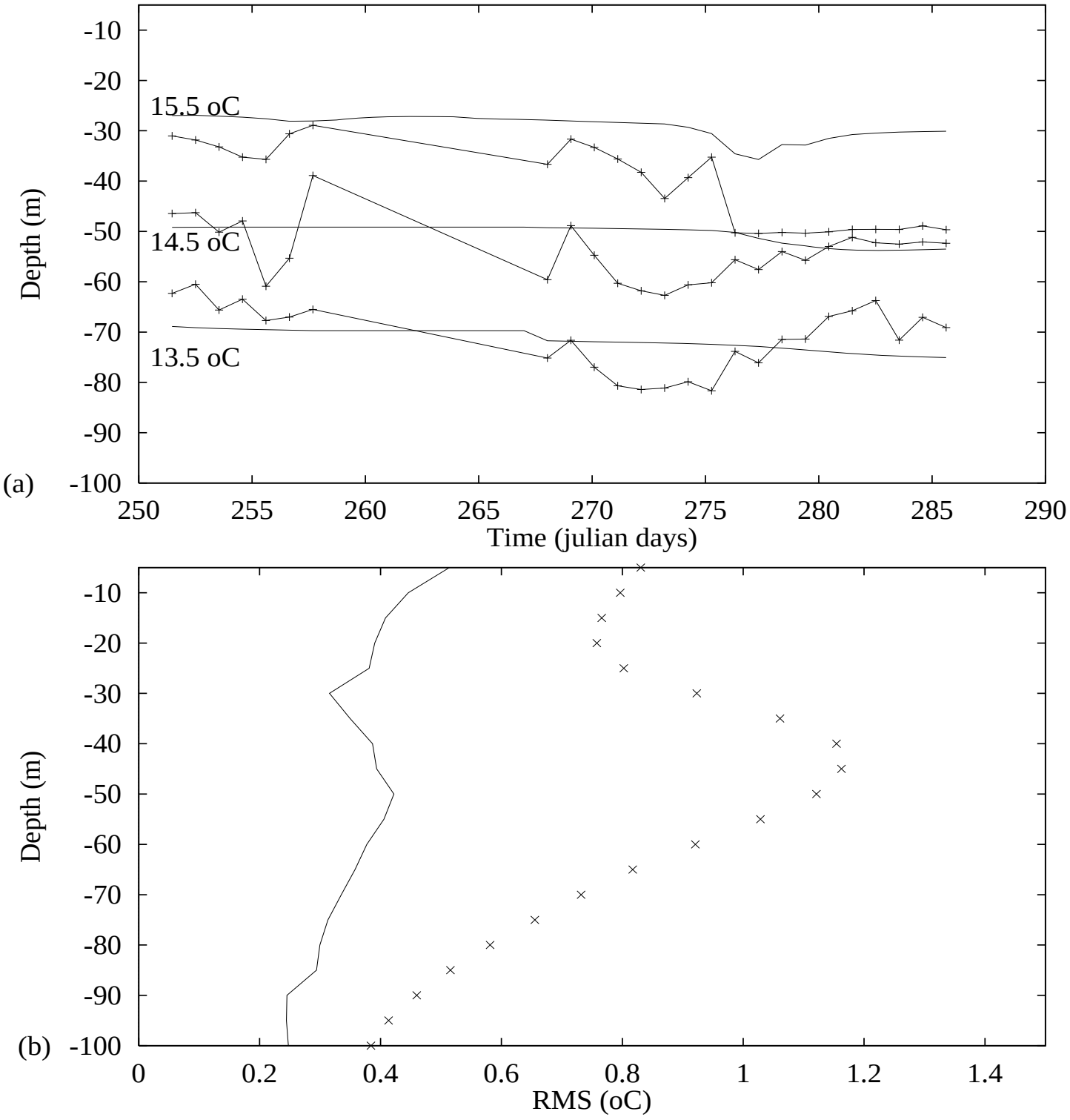
(a)
Depth (m)
-10
-20
-30
-40
-50
-60
-70
-80
-90
-100
15.5 oC
14.5 oC
13.5 oC
250
255
260
265
270
275
280
285
290
Time (julian days)
(b)
Depth (m)
-10
-20
-30
-40
-50
-60
-70
-80
-90
-100
0
0.2
0.4
0.6
0.8
1
1.2
1.4
RMS (oC)

Figure 19:

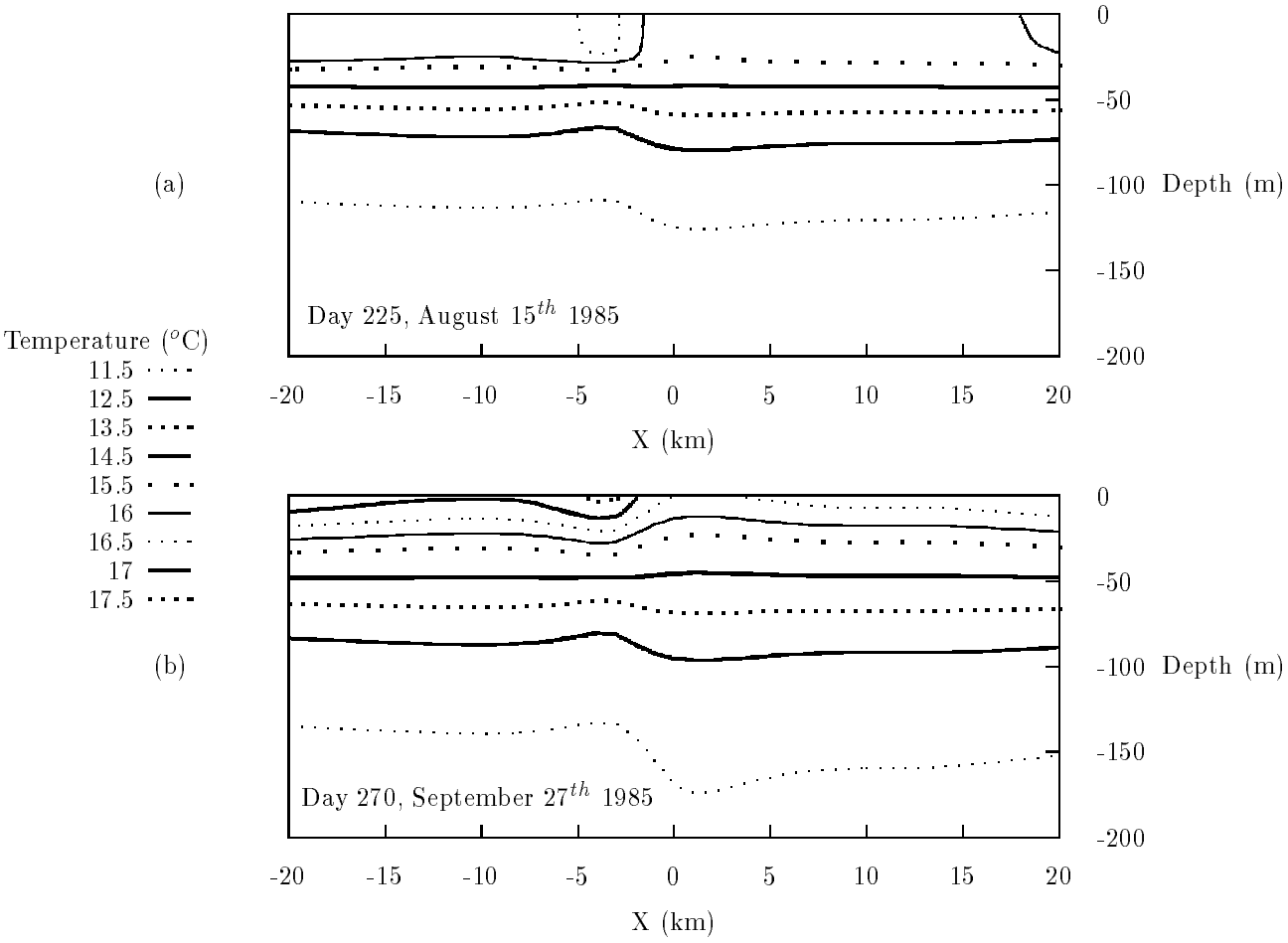
(a)
Day 225, August 15th 1985
Temperature (°C)
11.5
12.5
13.5
14.5
15.5
16
16.5
17
17.5
0
-50
-100
-150
-200
Depth (m)
-20
-15
-10
-5
0
5
10
15
20
X (km)
(b)
Day 270, September 27th 1985
0
-50
-100
-150
-200
Depth (m)
-20
-15
-10
-5
0
5
10
15
20
X (km)

Figure 20:

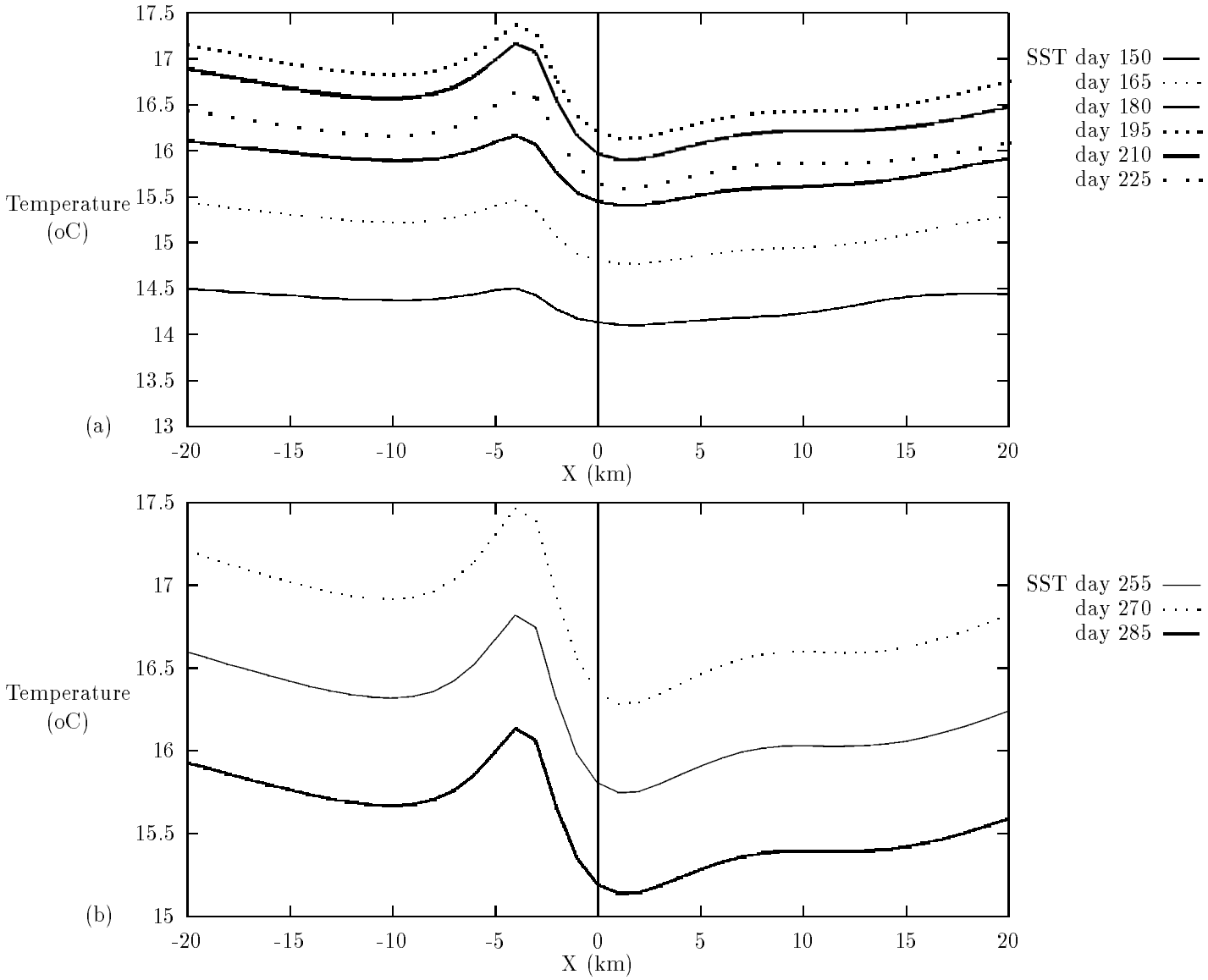
17.5
17
16.5
16
15.5
15
14.5
14
13.5
13
Temperature
(oC)
(a)
-20
-15
-10
-5
0
5
10
15
20
X (km)
SST day 150
day 165
day 180
day 195
day 210
day 225
17.5
17
16.5
16
15.5
15
Temperature
(oC)
(b)
-20
-15
-10
-5
0
5
10
15
20
X (km)
SST day 255
day 270
day 285

Figure 21:

(a)

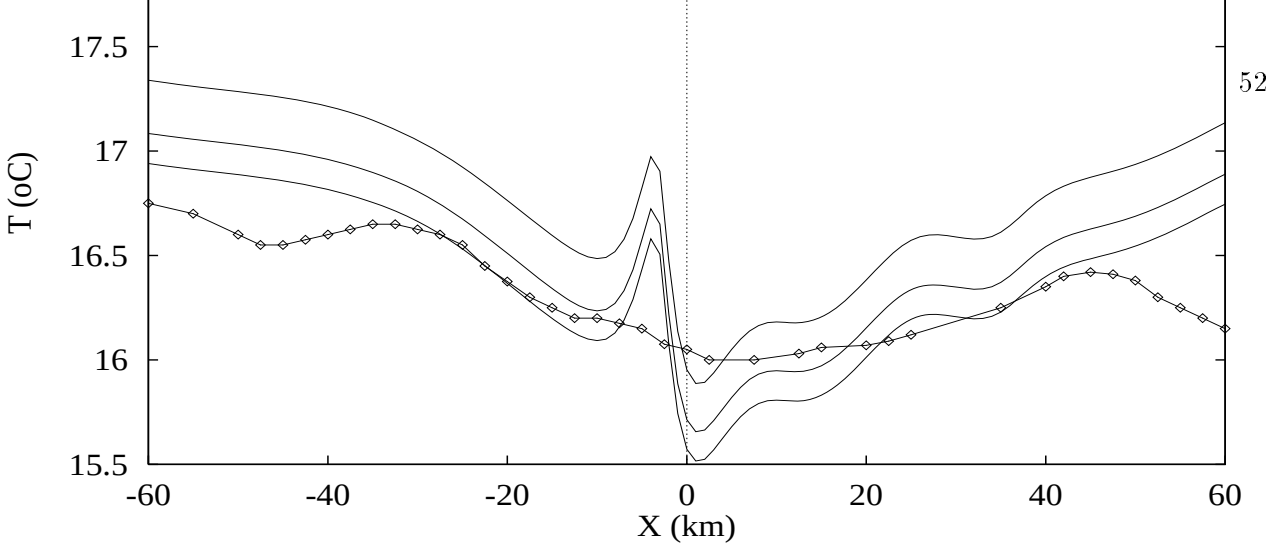

(b)

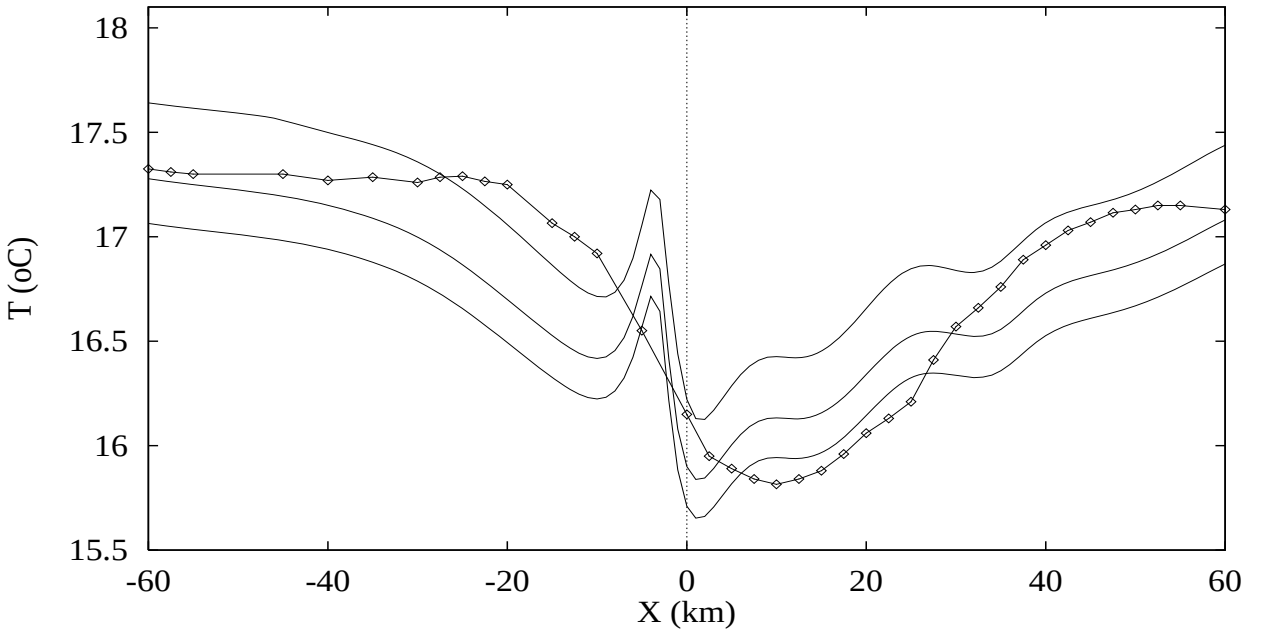

(c)

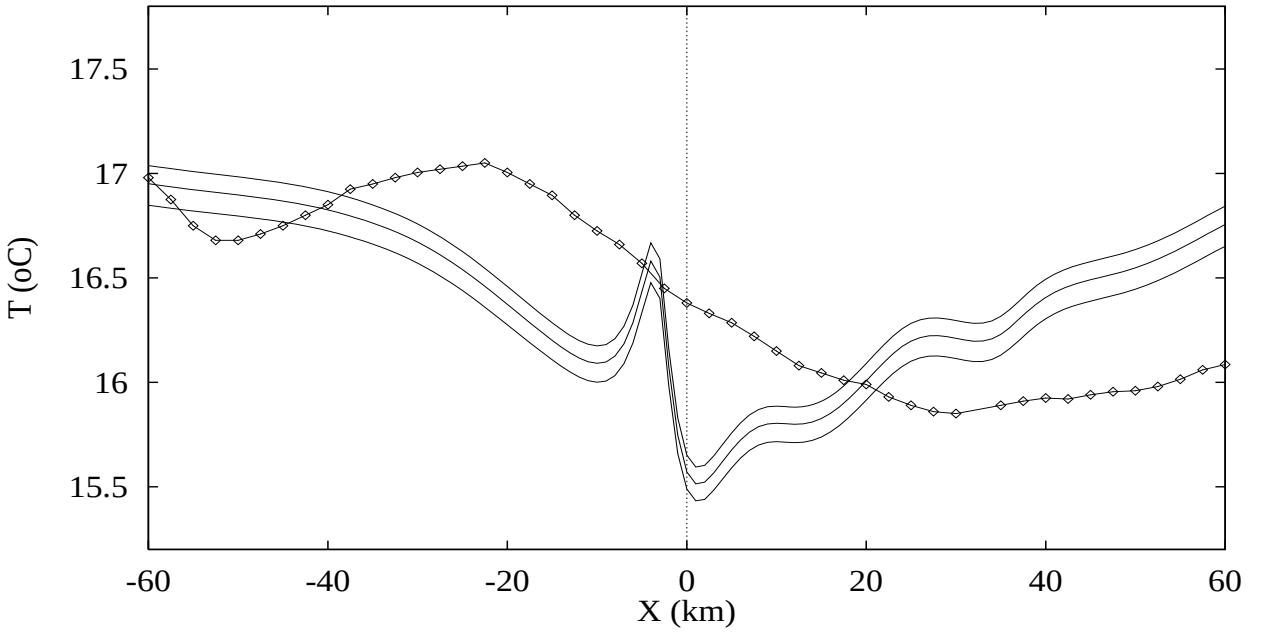

Figure 22: